

Fluid P-T-X characteristics and evidence for boiling in the formation of the Phoenix uranium deposit (Athabasca Basin, Canada): Implications for unconformity-related uranium mineralization mechanisms

Kewen Wang^a, Guoxiang Chi^{a,*}, Kathryn M. Bethune^a, Zenghua Li^a, Nigel Blamey^b, Colin Card^c, Eric G. Potter^d, Yongxing Liu^e

^a Department of Geology, University of Regina, Regina, Saskatchewan, Canada

^b Department of Earth Sciences, Western University, London, Ontario, Canada

^c Saskatchewan Geological Survey, Regina, Saskatchewan, Canada

^d Geological Survey of Canada, Ottawa, Ontario, Canada

^e Denison Mines Corp., Saskatoon, Saskatchewan, Canada

ARTICLE INFO

Keywords:

Fluid inclusions
Unconformity-related uranium deposits
Fluid boiling
Phoenix deposit
Athabasca basin

ABSTRACT

The Phoenix uranium deposit in the southeastern Athabasca Basin (Canada) is a typical unconformity contact-hosted uranium deposit, characterized by an association with reactivated basement faults, graphite-rich rocks in the underlying basement, and a pervasive clay alteration halo surrounding the mineralized zones. Petrographic results suggest that the mineralizing hydrothermal system was characterized by alternating desilicification and silicification events. Uraninite and clay-size minerals (tourmaline, kaolinite, illite and minor chlorite) mainly precipitated in the desilicification periods whereas hydrothermal quartz (mainly drusy quartz) formed during the silicification periods. Primary fluid inclusions in the hydrothermal quartz are inferred to represent the ore-forming fluids even though quartz did not co-precipitate with uraninite. The coexistence of multiple types of fluid inclusions (liquid-dominated biphasic, vapor-dominated biphasic, vapor-only and halite-bearing triphasic) within individual fluid inclusion assemblages is interpreted to indicate fluid boiling and heterogeneous trapping. Bulk fluid inclusion volatile analysis by mass spectrometry indicates H₂O as the dominant species, with less than 1 mol% non-aqueous volatiles that show a compositional trend typical of fluid boiling. Microthermometric and cryogenic Raman spectroscopic analyses indicate that the mineralizing fluids are of H₂O-NaCl-CaCl₂ ± MgCl₂ composition, with salinities ranging mainly from 23.4 to 31.1 wt%. The liquid-dominated biphasic inclusions (excluding those interpreted to have resulted from heterogeneous trapping) have homogenization temperatures from 90 to 157 °C. These data are generally consistent with the classical diagenetic-hydrothermal model in which basinal brines that extracted uranium from the basin or the basement were channeled along reactivated basement faults, and precipitated uraninite near the unconformity through reaction with reducing agents. However, the relatively low fluid inclusion homogenization temperatures documented in this paper, together with fluid boiling inferred from fluid inclusion assemblages, suggest that the deposit may have formed in a shallower environment (~2.5 km) than assumed in the conventional diagenetic-hydrothermal model (> 5 km). Abrupt fluid pressure drops during episodic faulting may have resulted in fluid boiling (flash vaporization) changing the fluid pH and promoting uraninite precipitation, with the alternating liquid-vapor conjugates of the boiling system resulting in alternating precipitation of quartz and uraninite respectively.

1. Introduction

Unconformity-related uranium deposits associated with Proterozoic sedimentary basins, especially those in the Athabasca and Thelon Basins in northern Canada and the Kombolgie Basin in northern

Australia, are among the richest and largest uranium deposits in the world (Jefferson et al., 2007; Kyser and Cuney, 2015). These deposits occur near the unconformity between the basin and basement and are associated with reactivated basement faults crosscutting the unconformity. They are generally considered to have formed from basinal

* Corresponding author.

E-mail address: guoxiang.chi@uregina.ca (G. Chi).

<https://doi.org/10.1016/j.oregeorev.2018.07.010>

Received 2 December 2017; Received in revised form 8 July 2018; Accepted 16 July 2018

Available online 21 July 2018

0169-1368/ © 2018 Elsevier B.V. All rights reserved.

brines derived from evaporated seawater (Richard et al., 2011, 2013, 2014; Mercadier et al., 2012), under “diagenetic-hydrothermal” conditions (Hoeve and Sibbald, 1978; Pagel et al., 1980; Hoeve and Quirt, 1984; Kotzer and Kyser, 1995; Derome et al., 2005; Richard et al., 2016), and at burial depths of > 5 km (Pagel, 1975; Pagel et al., 1980; Hoeve and Quirt, 1984; Kotzer and Kyser, 1995; Derome et al., 2005). However, a few fluid inclusions studies of uranium deposits associated with the Kombolgie Basin in northern Australia (Wilde et al., 1989) and the Thelon (Chi et al., 2017) and Martin Lake (Liang et al., 2017) basins in northern Canada, and a review of regional geochrono-stratigraphic data of the Athabasca Basin (Chi et al., 2018), suggest that the uranium deposits associated with the Proterozoic basins may have formed at shallower depths than previously thought (Chi et al., 2015, 2018; Chi and Chu, 2016). These studies reported the coexistence of vapor-only, vapor-dominated and liquid-dominated fluid inclusions reflecting fluid immiscibility or boiling, which in turn was interpreted to indicate low fluid pressures and shallow depths of mineralization (Wilde et al., 1989; Chi et al., 2017; Liang et al., 2017). Fluid boiling has also been reported for HREE-xenotime mineralization sharing similarities with unconformity-related uranium deposits in the Browns Range district in northwestern Australia (Richter et al., 2018).

Occurrences of vapor-only and vapor-dominated fluid inclusions have been previously reported in unconformity-related uranium deposits in the Athabasca Basin (Dubessy et al., 1988; Derome et al., 2005), but the significance in terms of fluid boiling and low fluid pressure was not recognized at the time. Chi et al. (2014a) reported fluid inclusion evidence for fluid boiling or immiscibility for a few unconformity-related uranium deposits in the Athabasca Basin, but detailed petrographic and microthermometric data were not provided. Fluid boiling was inferred from a detailed fluid inclusion study for the Maw Zone REE deposit in the Athabasca Basin (Rabiei et al., 2017), but this deposit, although interpreted to be related to unconformity-related uranium mineralization systems in the region, is actually poor in uranium (Rabiei et al., 2017). Thus, a detailed study documenting fluid inclusion assemblages indicative of fluid boiling or immiscibility, such as the one by Chi et al. (2017) for the End deposit associated with the Thelon Basin, is dearly lacking for unconformity-related uranium deposits associated with the Athabasca Basin, which is by far the most important setting for this type of uranium deposit.

In this paper, we report a detailed petrographic and fluid inclusion study of the Phoenix uranium deposit in the southeastern Athabasca Basin (Fig. 1A) which shows evidence of fluid boiling. The deposit, with an indicated resource of 166,400 tonnes of ore at an average grade of 19.13% U_3O_8 (Roscoe, 2014), is one of the richest uranium deposits in the world. It is situated between the world-class Key Lake and McArthur River deposits (Fig. 1A) and possesses geological characteristics typical of classical unconformity-related uranium deposits: an association with reactivated basement faults where they intersect the unconformity surface, graphite-rich rocks in the basement, and a pervasive clay alteration halo (Jefferson et al., 2007; Kerr, 2010; Kyser and Cuney, 2015). The abundance of drusy quartz, inferred to be related to mineralization based on its spatial association with mineralization, and the presence of fluid inclusions within this quartz, make this deposit ideal for studying the P-T-X conditions of the mineralizing fluids. In this study, the paragenesis of the mineral phases and events related to mineralization was first established through detailed petrographic study of polished thin sections. This was followed by detailed investigation of fluid inclusions themselves to establish the types, modes of occurrences, and timing relationships. Microthermometric studies of selected fluid inclusion populations were then carried out, followed by cryogenic Raman spectroscopic studies of solute compositions and mass spectrometric analyses of volatile compositions of bulk fluid inclusions. Based on these results, the fluid P-T-X conditions were calculated, which forms the basis for interpretation and discussion of mineralization conditions and processes, in particular fluid boiling. Furthermore, the significance of the study results for understanding the hydrodynamic

processes of mineralization and ore precipitation mechanisms is elucidated.

2. Geological setting

2.1. Regional geology

The Phoenix uranium deposit is one of many uranium deposits located in the eastern part of the Athabasca Basin (Fig. 1A), which comprises Paleo- to Mesoproterozoic sedimentary rocks overlying Archean to Paleoproterozoic crystalline basement rocks (Ramaekers et al., 2007; Card et al., 2007). The basement rocks underlying this part of the basin are part of the Hearne Province, which consists of, from west to east, the Virgin River, Mudjatik, Wollaston and Peter Lake domains (Fig. 1A).

The Wollaston Domain, which underlies the Phoenix uranium deposit, is composed of Paleoproterozoic metasedimentary rocks (mainly pelites) of the Wollaston Supergroup that are interfolded with Archean granitoid gneisses, along with small mafic to felsic intrusive bodies of unknown ages (Annesley et al., 2005; Card et al., 2007; Yeo and Delaney, 2007). Most of the basement rocks of the Wollaston Domain have been strongly deformed and metamorphosed during the Trans-Hudson orogeny (Hoffman, 1988), which resulted in tight to isoclinal northeast-trending doubly-plunging folds and thrust structures and upper amphibolite- to lower granulite-facies metamorphism (Annesley et al., 2005; Card et al., 2007; Yeo and Delaney, 2007).

The Athabasca Basin is filled with sedimentary rocks designated as the Athabasca Group, which were deposited from ca. 1760 to 1500 Ma, during the waning stages of the Trans-Hudson orogeny and afterward (Ramaekers et al., 2007). The Athabasca Group comprises four unconformity-bounded sequences, which are, from bottom to top, the sandy to conglomeratic Fair Point Formation (sequence 1), the quartz-arenitic Read, Smart and Manitou Falls formations (sequence 2), the pebbly sandy Lazenby Lake and mudstone-rich Wolverine Point formations (sequence 3), and the pebbly to sandy and conglomeratic Locker Lake, sandy Otherside, mudstone-rich Douglas, and dolomitic Carswell formations (sequence 4) (Ramaekers et al., 2007). In the eastern part of the Athabasca Basin, the lowermost sequence (Fair Point Formation) is absent, and the uppermost sequence has been eroded (Ramaekers et al., 2007).

2.2. Geology of the Phoenix uranium deposit

The Phoenix uranium deposit is situated in the southeastern Athabasca Basin, about 35 km southwest of the McArthur River deposit and 25 km northeast of the Key Lake deposit (Kerr, 2010) (Fig. 1A). The mineralization occurs at the contact between the Athabasca Group and the underlying basement rocks and is closely associated with reactivated basement faults (Fig. 1B and C).

The basement rocks at Phoenix are metasedimentary rocks of the Wollaston Supergroup including graphitic and non-graphitic pelitic gneiss, semipelitic gneiss, quartzite, rare felsic and quartz feldspathic granitoid gneiss and calc-silicate gneiss (Fig. 1B and C). Note that the graphite in the graphitic pelitic gneiss has been generally considered to have originated from metamorphism of carbonaceous material in metasedimentary rocks (e.g., Buseck and Beyssac, 2014), but new field and petrographic observations suggest that much of it in the basement rocks of the Athabasca Basin may be of hydrothermal origin (Card, 2012). In this paper we use “graphitic pelitic gneiss” as a descriptive term without considering origin of the graphite. The top 3–10 m of the basement rocks immediately below the unconformity are superimposed by a paleo-weathering and alteration profile that has been reported throughout the basin (MacDonald, 1985; Cuney et al., 2003; Kerr, 2010). The pelitic units typically contain garnet, cordierite and sillimanite, indicative of upper amphibolite- to lower granulite-facies metamorphism. Decimeter- to meter-thick, sheet-like quartz-rich pegmatite segregations are commonly present in all the metasedimentary

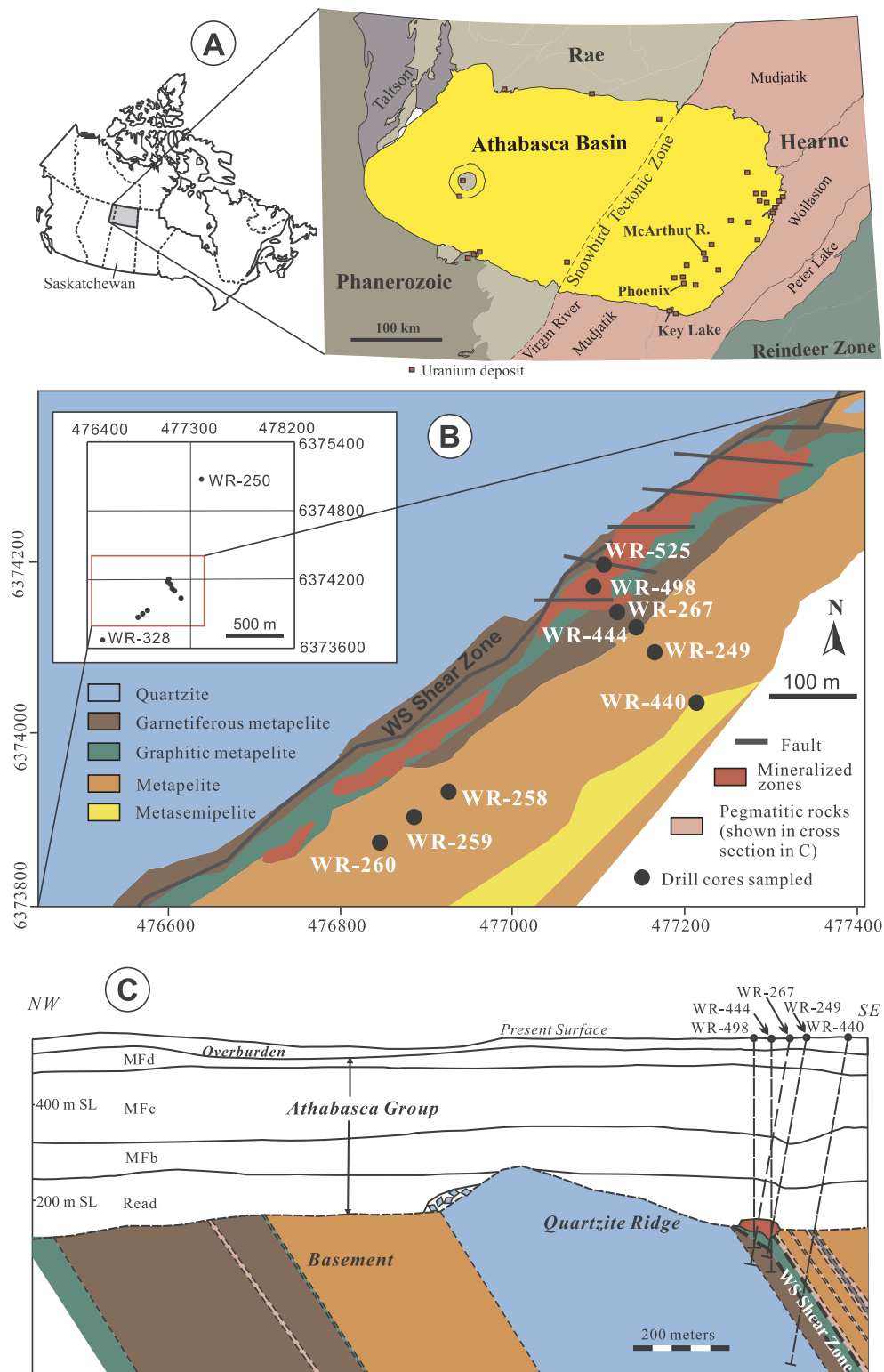


Fig. 1. A. Location of the Athabasca Basin in the regional tectonic framework of northern Saskatchewan (modified from Card et al., 2007). B. Basement geology of the Phoenix deposit and locations (collar) of diamond drill holes examined in this study (modified from Roscoe, 2014). C. Schematic cross section of the Phoenix deposit and neighboring area (modified from Arseneau and Revering, 2010). Sandstone units: Rd = Read Formation, MF = Manitou Falls Formations: MFb = Bird Member, MFc = Collins Member, MFd = Dunlop Member.

units. A prominent paleo-topographic ridge (basement high) composed of massive quartz occurs immediately on the west side of the Phoenix deposit (Fig. 1B and C) (Li et al., 2015). This massive quartz body, and many quartz-dominated units within the Wollaston Group in the region, were previously interpreted as quartzite with the connotation of a

metasedimentary origin (e.g. Yeo and Delaney, 2007). However, gradational relationships and pseudomorphic textures between these quartz-rich lithologies and pegmatite as well as pelitic gneiss have led Card (2012) to propose that the so-called quartzite is of hydrothermal origin. In this paper, we still use “quartzite” for the quartz-rich layers

and “quartzite ridge” for the massive quartz ridge, as in the literature, without considering the origin.

The sedimentary rocks above the unconformity comprise the Read Formation at the base and the Manitou Falls Formation above it. The preserved thickness of the two formations varies from ~170 m over the quartzite ridge to ~560 m on the west side of the ridge (Kerr, 2010; Roscoe, 2014). The Read Formation thins towards the “quartzite ridge” and wedges out over the top (Fig. 1C). Fault-scarp talus breccias consisting of centimeter- to meter-size angular quartzite blocks have been observed on the west side of the quartzite ridge within the Read Formation (Bosman and Korness, 2007; Fig. 1C). The overlying Manitou Falls Formation is composed mainly of sandstone and is divided into three members, i.e., from bottom to top, the Bird (MFb), Collins (MFc) and Dunlop (MFD) members based on the content of conglomerates and clay intraclasts (Bosman and Korness, 2007; Fig. 1C).

The WS shear zone, which is associated with the uranium mineralization at Phoenix, strikes northeast and dips moderately to the southeast (Fig. 1B and C). It is rooted in the graphite-rich pelitic units in the basement and crosscuts the unconformity, displaying a minor reverse offset. This deformation zone is characterized by development of a strong gneissic/migmatitic foliation superimposed by spaced, ductile to brittle deformation and fracturing/cataclasis in localized zones (Kerr, 2010). Drusy quartz-filled fracture networks, with local zones of brecciation, cut the basement, sandstone and the unconformity surface. The drusy quartz is widely developed in the sandstones near the mineralized zones (Fig. 2), and it is locally developed in the basement immediately below the unconformity.

The uranium mineralization at Phoenix occurs at the intersection between the WS shear zone and the unconformity (Fig. 1C). The mineralized zones appear to slightly widen where EW- or WEW-trending faults intersect the NE-trending WS shear zone (Fig. 1B). The mineralized bodies occur as shallowly dipping lenses that are mostly hosted by the lowermost Athabasca Group above the unconformity (but may extend for a few meters into the basement). In places, the unconformity-hosted ore zone is composed of several thin, stacked mineralized zones. Minor basement-hosted mineralization forms steeply dipping, discontinuous, thin, and parallel to sub-parallel mineralized zones along the faults associated with the WS shear zone.

The mineralized zones are surrounded by an alteration halo characterized by desilicification, clay-size minerals and silicification. Desilicification and clay alteration are closely related to each other and are best developed in proximity to the mineralized zones (Fig. 2A), whereas silicification is mainly developed in the host sandstone further away from the mineralized zones and in intervals between desilicified zones. Desilicification is manifested by disintegration of sandstone into loose grains (Fig. 2A), and clay alteration is characterized by pervasive clay-sized tourmaline, kaolinite and illite, and minor amounts of chlorite. The clay-sized tourmaline also occurs in fractures in the sandstone (Fig. 2B). This tourmaline has generally been referred to as dravite in the literature, but recent studies indicate that it has a composition of magnesiofoitite (Rosenberg and Foit, 2006; O’Connell et al., 2015; Adlakha and Hattori, 2016). In this paper, we use the general term “tourmaline” for consistency. The dominance of tourmaline in the proximal alteration zone at Phoenix is in contrast with the dominance of illite with lesser amounts of dickite in the area (Earle and Sopuck, 1989; Cloutier et al., 2010), as is also found in the nearby Maw Zone REE deposit (Rabiei et al., 2017).

Silicification is manifested as quartz cementation, especially drusy quartz filling fractures and dissolution vugs (Fig. 2C to E). Tourmaline also occurs around and within the drusy quartz veins (Fig. 2C). The drusy quartz crystals are euhedral, equant or blade-like, show comb textures, and vary from 2 to 3 mm up to around 1 cm in length (Fig. 2C and D). Many of the quartz crystals are corroded, as evidenced by holes within the crystals (Fig. 2D). Disseminated euhedral pyrite is locally developed coating the drusy quartz grains in sandstone (Fig. 2E).

3. Sampling and study methods

A number of samples were collected from drill cores in the Phoenix deposit area (Fig. 1B and C), with some from the Athabasca sandstone and some from the basement. All the samples examined in this study are from the clay-altered Athabasca sandstone surrounding the mineralization, with an emphasis on those that contain drusy quartz suitable for fluid inclusion study (Fig. 2). The samples from the basement were excluded from this study because few of them contain workable fluid inclusions and the timing relationship between the host mineral (quartz) and mineralization is more difficult to determine.

Polished thin sections were made from the samples for petrographic study, and doubly polished sections about 100 μm thick were made for fluid inclusion study. Optical examination of polished thin sections was completed on an Olympus BX51 petrographic microscope that is equipped with both transmitted and reflected light attachments. A scanning electron microscope (JEOL JSM-6360) equipped for energy dispersive spectroscopy (Thermo Scientific Noran System 7) (SEM-EDS) was used as an auxiliary tool to characterize fine-grained minerals.

Microthermometry was carried out using a Linkam THMSG 600 Heating/Freezing stage attached to an Olympus BX51 petrographic microscope at the Geofluids Laboratory of the University of Regina. The stage was calibrated with synthetic standard fluid inclusions of H_2O with an ice-melting temperature of 0°C and critical temperature of 374.1°C , and fluid inclusions of $\text{H}_2\text{O}-\text{CO}_2$ with a CO_2 -melting temperature of -56.6°C . The fluid inclusions were classified based on phase assemblages at room temperature, and the fluid inclusion assemblage (FIA) concept (Goldstein and Reynolds, 1994) was used to constrain the consistency of microthermometric data and the relationships between different types of fluid inclusions. Fluid inclusions that are distributed within a growth zone, along a healed fracture that does not extend beyond the edge of a crystal, or in a small cluster within a microdomain in a crystal, are considered to be primary or pseudo-secondary and treated as an FIA (Chi and Lu, 2008). The aqueous fluid inclusions are approximated by the $\text{H}_2\text{O}-\text{NaCl}-\text{CaCl}_2$ system, and the salinity ($\text{NaCl} + \text{CaCl}_2$ wt%) and X_{NaCl} values ($\text{NaCl}/(\text{NaCl} + \text{CaCl}_2)$ weight ratios) were determined with a Microsoft® Excel©-based computer program by Steele-MacInnis et al. (2011).

Raman spectroscopic analysis was carried out with a Renishaw RM2000 laser Raman spectroscope at the Geofluids Laboratory, University of Regina. The excitation laser wavelength is 514 nm, the grating is 1800, and the objective is $\times 50$ with a long working distance. Fluid inclusion chips were put in the Linkam THMSG 600 Heating/Freezing stage connected to a Leica DMLM petrographic microscope that is attached to the Raman system, and Raman spectroscopic analysis was conducted at room temperature (for gas composition of the vapor phase) or at -185°C (cryogenic Raman analysis for solute composition). The cryogenic Raman analysis follows the procedure as described by Chu et al. (2016): the aqueous inclusions were initially cooled at a rate of 30°C per minute to -185°C , at which the Raman spectra indicated only ice was nucleated; then the inclusions were warmed at 2°C per minute to promote the crystallization of hydrates, until clear spectra of hydrates could be detected by Raman, generally at -75°C for the inclusions examined in this study; finally, the fluid inclusions were cooled rapidly to -185°C again at $30^\circ\text{C}/\text{min}$ and maintained at -185°C for Raman spectroscopic examinations. Data were collected between 3000 and 3800 cm^{-1} , which covers all the peaks of ice and hydrates in the $\text{H}_2\text{O}-\text{NaCl}-\text{CaCl}_2$ system (Baumgartner and Bakker, 2010). Six acquisitions of 10 s each were carried out for each spot for a given fluid inclusion; as many as five spots of each individual fluid inclusion were analyzed (depending on the size) to check for consistency.

Bulk fluid inclusions were analyzed from pure concentrates of drusy quartz to obtain quantitative volatile compositions of fluid inclusions. The selected hand sample was crushed to millimeter-size particles with a rock hammer, and quartz grains were handpicked and cleaned with an

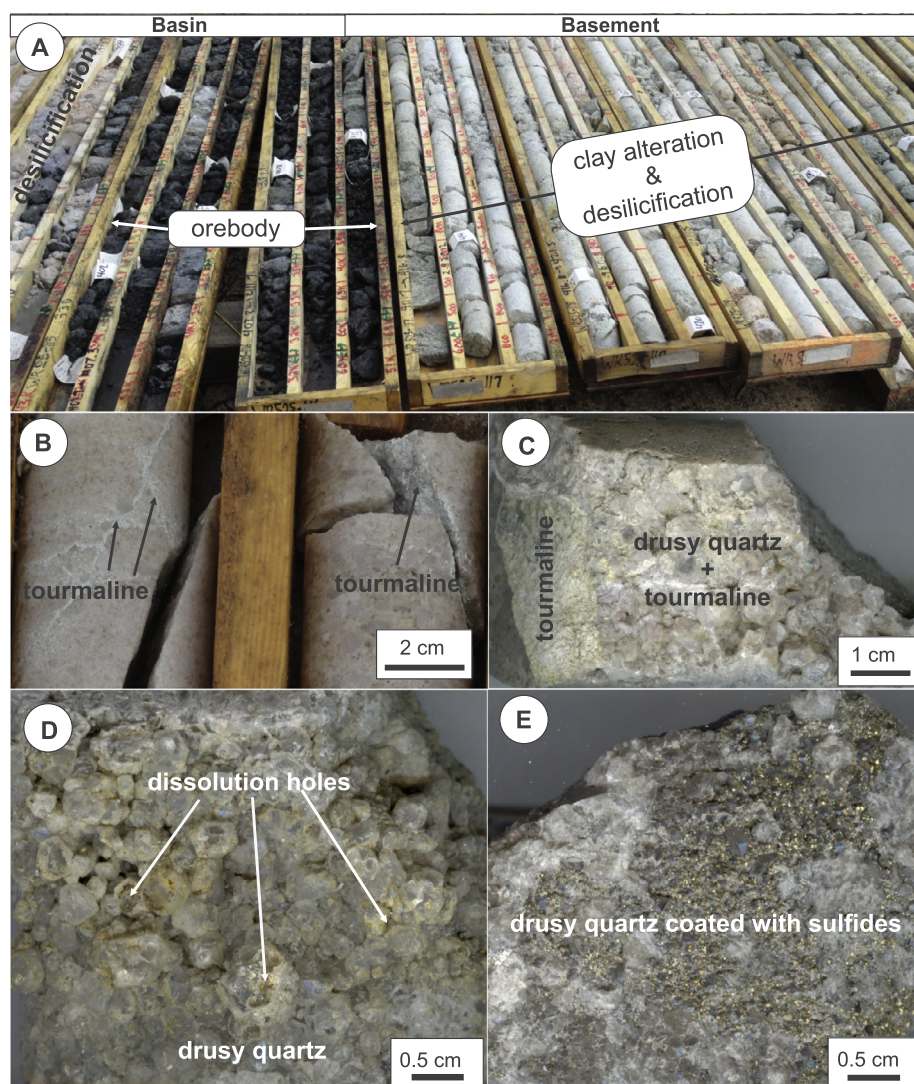


Fig. 2. Photographs of drill cores from the Phoenix deposit. A. Massive uranium ore zone surrounded by clay alteration and desilicification halo (DDH WR-525); B. Tourmaline coating fractures in the sandstone (DDH WR-328); C. Drusy quartz + tourmaline filling a fracture in the sandstone which is altered by tourmaline (DDH WR-328, 332.4 m); D. Drusy quartz crystals with abundant dissolution cavities (DDH WR-328, 326.8 m); E. Drusy quartz coated with sulfide minerals (DDH WR-328, 369.8 m).

ultrasonic bath in a KOH solution to remove surface contamination. The dry and clean samples were then sent to New Mexico Institute of Mining and Technology for mass spectrometry analysis. The quartz samples were crushed incrementally under high vacuum, producing 4–10 successive bursts, which were then analyzed by two Pfeiffer Prisma quadrupole mass spectrometers operating in fast-scan, peak-hopping mode (Blamey, 2012; Blamey et al., 2015). Scott Gas standard gas mixtures of known compositions (2% uncertainty) and three in-house water-gas standards were employed for calibration. Accuracy estimated from analysis of air encapsulated in capillary tubes is 0.4% for N_2/Ar ratio. Analytical precisions are better than 5% for major gas species (CO_2 , CH_4 , N_2 , and Ar) and 10% for minor species (Blamey, 2012). The 2- σ detection limits range from 0.00002 to 0.00003% (i.e., 0.2 to 0.3 ppm) based on the formula described in Blamey et al. (2012, 2015).

Fluid pressures and isochores for aqueous inclusions in drusy quartz were calculated with the FLUIDS package (Bakker, 2003). The homogenization temperature (T_h) and salinity values were used to calculate bulk fluid density and homogenization pressure (P_h) with the “BULK” program (using the empirical equation of state of Bodnar, 1993), assuming a NaCl- H_2O fluid system. Then the Loner 9 program (Bakker, 2003) was employed to estimate the potential error in P_h introduced by

non-aqueous volatiles, using the equation of state by Duan et al. (1992a, b; 1996) for the H_2O - CO_2 system.

4. Petrography and paragenesis

The petrographic study is focused on quartz and tourmaline, the former being the host of fluid inclusions for study and the latter serving as link between the fluid inclusions and uranium mineralization. Four generations of quartz (labelled Qz0, Qz1, Qz2 and Qz3) and three generations of tourmaline (labelled Trm1, Trm2 and Trm3) were distinguished in the samples. The characteristics of these mineral phases and their timing relationships with other minerals associated with uranium mineralization, including illite, kaolinite, uraninite and sulfides are illustrated in Figs. 3–5 and described below.

Qz0 represents detrital quartz that makes up the bulk of the Athabasca Group sandstone. It is commonly cemented by quartz overgrowths (Qz1), separated by a “dustline” rich in iron oxide-hydroxide (IOH) (Fig. 3A). Qz1 is widespread in the Athabasca Group sandstone throughout the basin and is interpreted as a product of diagenesis. Diagenetic dickite and illite and locally chlorite are developed in the sandstones, but these minerals are not preserved in the samples from

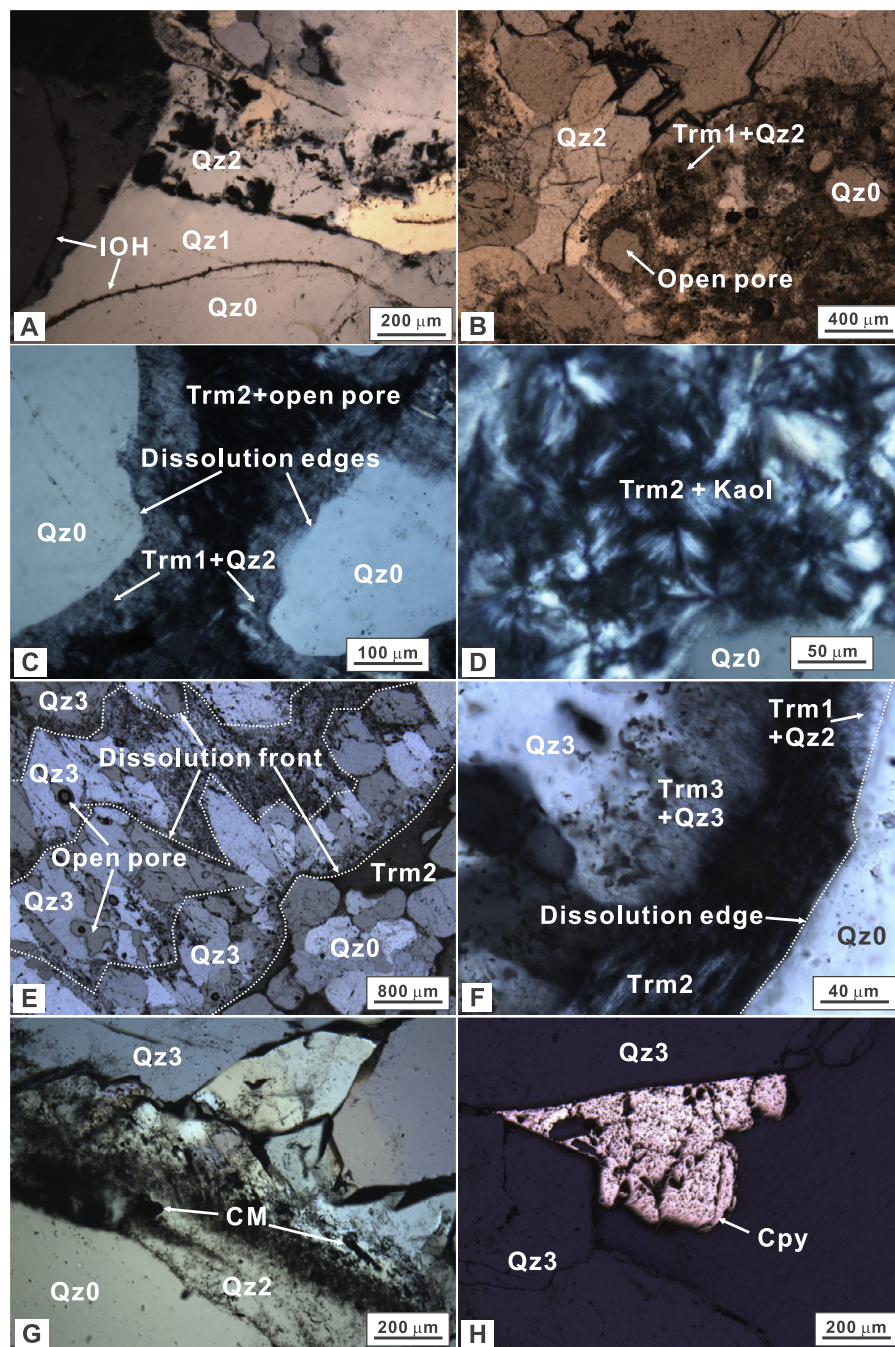


Fig. 3. Photomicrographs showing petrographic features of the sandstone surrounding the mineralized zones of the Phoenix deposit: A. Sandstone (Read Formation) with diagenetic quartz overgrowth (Qz1) surrounding detrital quartz (Qz0), separated by an iron oxide – hydroxide (IOH) dust-line, cemented by hydrothermal quartz (Qz2) (DDH WR-267, 338.4 m; XPL); B. Vug-filling quartz (Qz2) and tourmaline intergrowth (Trm1) followed by desilicification (DDH WR-328, 348.1 m; PPL); C. Detrital quartz with corrosive edge surrounded by syntaxial quartz (Qz2) intergrown with tourmaline (Trm1), followed by open space-filling tourmaline (Trm2) (DDH WR-328, 348.1 m; XPL); D. Open space-filling tourmaline (Trm2) (DDH WR-328, 348.1 m; XPL); E. Drusy quartz vein (Qz3) with multiple dissolution fronts and open pores (DDH WR-328, 304.1 m; PPL); F. Drusy quartz (Qz3) with intergrown tourmaline (Trm3) (DDH WR-328, 304.1 m; XPL); G. Amorphous carbonaceous materials (CM) along growth zone in hydrothermal quartz (DDH WR-328, 332.4 m; XPL); H. Chalcopyrite (Cpy) in growth contact with drusy quartz (Qz3) (DDH WR-328, 369.8 m; RFL).

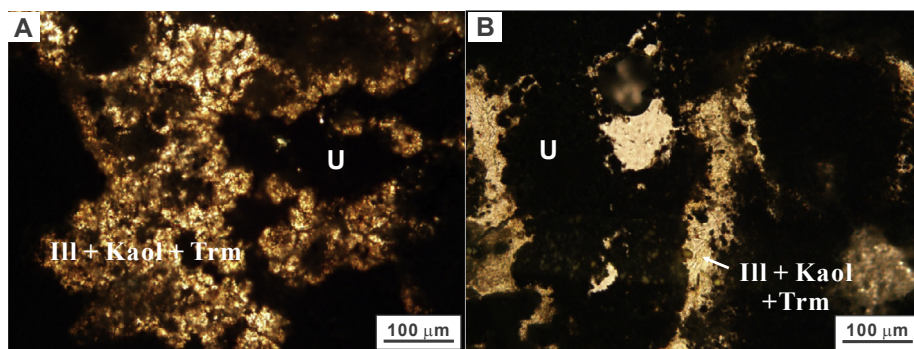


Fig. 4. A. Uraninite disseminated in mixtures of tourmaline, kaolinite and illite (DDH WR-437, depth 411.1 m); B. Massive uraninite ore associated with mixtures of tourmaline, kaolinite and illite (DDH WR-404, depth 415.5 m).

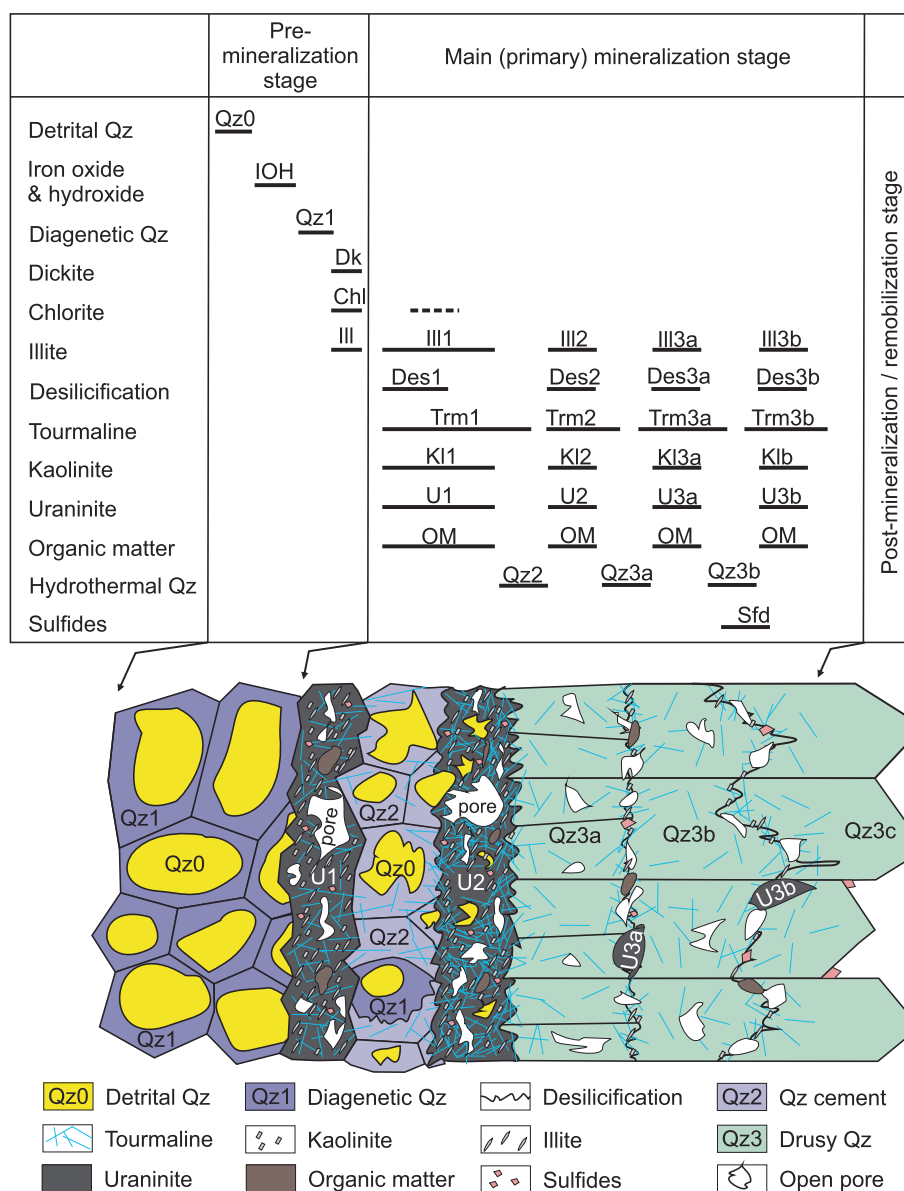


Fig. 5. Paragenetic sequence of minerals and events in relation to mineralization, with an interpretative sketch illustrating the crosscutting relationships between various mineral phases and events. Note, although the labeling of the events (e.g., U1, U2, U3) shown in this figure may suggest sequential timing, they are actually meant to be time-independent, and are just here used to illustrate the multi-episodic nature of the mineralization system; see more detailed explanation in the text.

the mineralization-associated alteration halo. Although Qz1 is locally preserved and enclosed by a second quartz overgrowth (Qz2) in the alteration halo surrounding the mineralized zones (Fig. 3A), it was mostly dissolved during the desilicification events associated with mineralization (Fig. 3B–G). As a result, Qz0 is in direct contact with later generations of quartz, separated by a dissolution edge (Fig. 3B–G). Qz2 is the first generation of hydrothermal quartz that occurs as the cement in breccia zones (involving Qz0 and Qz1) in sandstone (Fig. 3A–G). Qz2 is commonly associated with tourmaline (Trm1) and minor amounts of illite and kaolinite dispersed in the quartz crystals (Fig. 3B, C and F). A second generation of tourmaline (Trm2) in association with kaolinite developed in residual pores following Qz2 and Trm1, without associated quartz (Fig. 3C–F). Minor amounts of chlorite is present in the tourmaline-kaolinite-illite mixture in the alteration halo. The second generation of hydrothermal quartz (Qz3), in the form of drusy quartz in dissolution vugs and fractures, is separated from Qz0, Qz1 and Qz2 by dissolution features (Fig. 3E–G). Qz3 is also associated with tourmaline (Trm3) and commonly contains dissolution hollows and multiple dissolution fronts within a given vein (Fig. 3E). The dissolution fronts are

characterized by irregular edges of Qz3 and impurities including carbonaceous material (CM, Fig. 3G) and clay-size minerals. Qz3 is locally associated with sulfides (e.g., chalcopyrite) with straight (growth) contacts (Fig. 3H), suggesting co-precipitation.

Uraninite is closely associated with mixtures of tourmaline, kaolinite and illite (Fig. 4). The tourmaline in these mixtures, characterized by needle-like textures (Fig. 4), appears to be the same as those associated with drusy quartz (Fig. 3B–F), and cannot be clearly classified as Trm1, Trm2 or Trm3. No hydrothermal quartz (Qz2 or Qz3) was found in contact with uraninite.

Based on the crosscutting relationships described above and the observations that the mineralized zones are intimately associated with tourmaline + kaolinite + illite (and minor amounts of chlorite) alteration and desilicification (Fig. 2A), whereas drusy quartz is well developed in sandstones surrounding the ore zones but is not in direct contact with the ores, it is inferred that uraninite precipitation was contemporaneous with dissolution of quartz and precipitation of tourmaline, kaolinite and illite, whereas silicification (Qz2 and Qz3) took place in intervals between individual mineralization (and

desilicification) events. The hydrothermal quartz (Qz2 and Qz3), although not coprecipitated with uraninite, is considered to be formed in the same hydrothermal event as uraninite, tourmaline, kaolinite and illite, based on its close spatial association with uranium mineralization and its coprecipitation with tourmaline (Fig. 4).

The paragenetic sequence may be divided into three stages, i.e. pre-mineralization stage, main (primary) mineralization stage, and post-mineralization/remobilization stage – which is not covered in this study (Fig. 5). The detrital quartz (Qz0) and diagenetic quartz (Qz1), the iron oxide/hydroxide enclosed by Qz1 as well as diagenetic dickite, illite and chlorite belong to the pre-mineralization stage. The main (primary) mineralization stage is characterized by alternating episodes of 1) precipitation of uraninite, kaolinite, illite, and minor chlorite and organic matter, and dissolution of quartz, and 2) precipitation of quartz and some tourmaline. It should be noted that although the labeling of the events (e.g., U1, U2, U3) shown in Fig. 5 may suggest sequential timing, they are actually meant to be time-independent, and are used here to illustrate the multi-episodic nature of the mineralization system. Thus, a desilicification event recorded by the dissolution feature within the drusy quartz (e.g., the one associated with U3a in Fig. 5) may have been taking place (outside the mineralized zones) at the same time as massive uranium mineralization (e.g., U1 or U2 shown in Fig. 5) within the mineralized zones. Overall, Qz2-3, Trm1-3 (and associated kaolinite and illite) and U1-3 are considered to represent products of a unified and continuous hydrothermal system, rather than distinct hydrothermal systems separated by protracted periods of time.

5. Results

5.1. Fluid inclusion types and occurrences

Fluid inclusions were studied in Qz2 and mostly in Qz3. Four types of fluid inclusions (in both Qz2 and Qz3) were identified at room temperature, including liquid-dominated biphasic (liquid + vapor), vapor-dominated biphasic (vapor + liquid), monophasic (vapor-only), and triphasic (liquid + vapor + solid) inclusions (Fig. 6). Both the liquid-dominated biphasic inclusions and the vapor-dominated biphasic inclusions comprise a liquid phase and a vapor phase, the former having a vapor percentage < 50% (Fig. 6A) and the latter > 50% (Fig. 6B) at room temperature. The monophasic inclusions only consist of a vapor phase at room temperature, with no visible liquid phase (Fig. 6C). The triphasic inclusions are composed of a liquid phase, a vapor phase and a

halite crystal at room temperature (Fig. 6D). The sizes of fluid inclusions range from 2 to 20 μm .

In Qz2 and Qz3, the fluid inclusions are randomly distributed or occur as clusters along growth features. The growth features are manifested as a cloudy core populated with fluid inclusions surrounded by a clean rim (Fig. 7A) and as a band bounded by growth discontinuities (Fig. 7B). Fluid inclusions may occur along growth zones outlined by clarity or abundance fluid inclusions (Fig. 7C–E) or occur along short healed fractures within a growth zone (Fig. 7F). Different types of fluid inclusions commonly occur within the same growth zones (Fig. 7C–E) or the same short intracrystal healed fractures (Fig. 7F), suggesting fluid boiling (boiling rather than immiscibility is used based on the low concentrations of non-aqueous volatiles, see below) and heterogeneous trapping. Accordingly, we have inferred the following: 1) the liquid-dominated fluid inclusions with the lowest vapor percentage represent the homogeneously entrapped liquid phase; 2) the vapor-only inclusions represent the homogeneously entrapped vapor phase; and 3) the liquid-dominated fluid inclusions with relatively high vapor percentages and the vapor-dominated fluid inclusions represent heterogeneously entrapped liquid and vapor phases (Goldstein and Reynolds, 1994; Chi and Lu, 2008). Similarly, the triphasic inclusions are interpreted to have resulted from heterogeneously entrapped liquid and solid (halite) because these inclusions coexist with liquid-dominated biphasic inclusions (Fig. 7C and F). These inferences apply to fluid inclusions in both Qz2 and Qz3 based on their similarities in types of fluid inclusions and assemblages (Fig. 7).

5.2. Microthermometric results

Based on the interpretation of fluid boiling and heterogeneous trapping discussed above, the liquid-dominated biphasic inclusions with the lowest vapor percentage were prioritized for microthermometric measurements. Vapor-only inclusions could not be studied for microthermometry because the liquid phase that is presumably present (wetting the inclusion wall) was invisible. The other biphasic inclusions with variable vapor percentages likely resulted from heterogeneous trapping and so could not yield valid microthermometric data.

The microthermometric data of 357 primary or pseudosecondary liquid-dominated fluid inclusions representative of homogeneous trapping are listed in Table 1. Most of the data are from Qz3, as only a few workable fluid inclusions (8 inclusions in one FIA) were found in Qz2. A few triphasic inclusions were analyzed despite being interpreted as

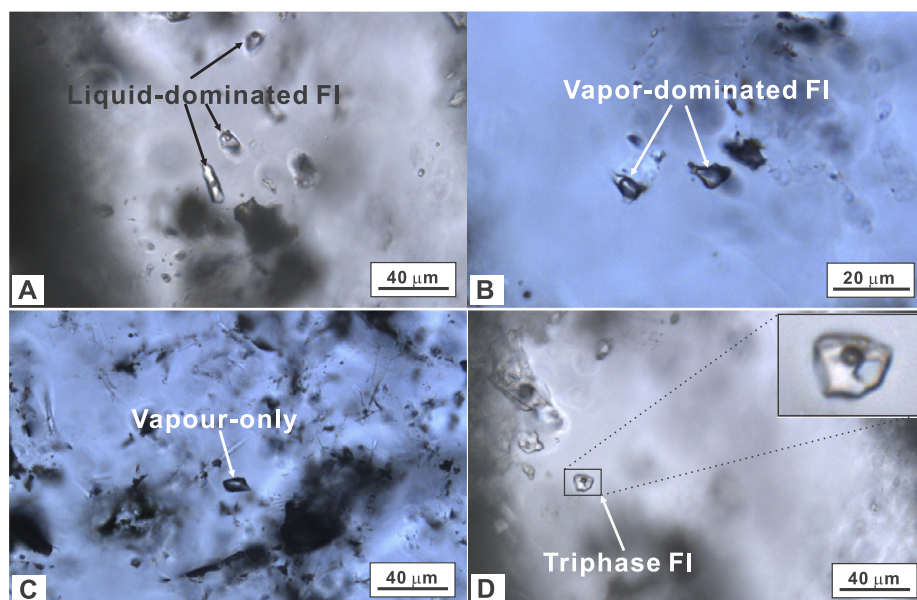


Fig. 6. Photomicrographs of different types of fluid inclusions (all in PPL): A. Liquid-dominated biphasic (liquid + vapor) inclusion in Qz3 (DDH WR-250, 341.8 m); B. Vapor-dominated biphasic (vapor + liquid) inclusions in Qz3 (DDH WR-328, 326.8 m); C. Monophasic (vapor-only) inclusion in Qz3 (DDH WR-328, 369.8 m); D. Triphasic (liquid + vapor + solid) inclusion in Qz3 (DDH WR-250, 341.8 m).

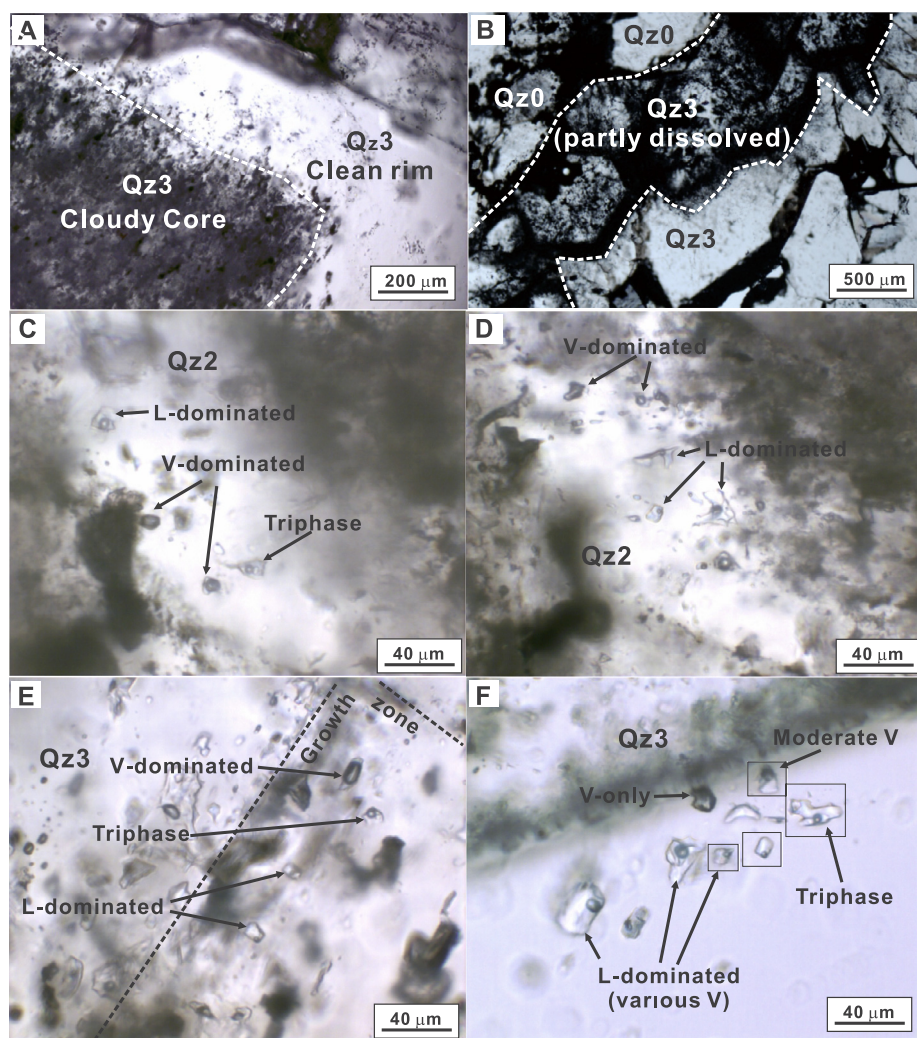


Fig. 7. Photomicrographs of a sample from DDH WR-328 (at 326.8 m) showing various occurrences of aqueous fluid inclusions and co-existence of liquid-dominated and vapor-only fluid inclusions as well as fluid inclusions with variable vapor/total ratios within individual fluid inclusion assemblages (all in PPL). A. Drusy quartz (Qz3) with a cloudy core (with abundant fluid inclusions) surrounded by relatively inclusion-free growth zone; B. A cloudy growth zone in drusy quartz (Qz3) bounded by dissolution features; C and D. Co-existence of different types of fluid inclusions in growth zones in Qz2. E. Co-existence of different types of fluid inclusions in a growth zone in Qz3. F. A short trail of fluid inclusions distributed along the growth direction in Qz3. Note fluid inclusions enclosed in rectangles were brought to focus from different depths in the doubly polished sections.

resulting from heterogeneous trapping, for the purpose of comparison with the liquid-dominated inclusions. The data of these triphase inclusions are listed in Table 1, but they are not included in the statistical analysis and diagrams (Figs. 8–10). The analyzed fluid inclusions are divided into two categories: isolated fluid inclusions, and fluid inclusions that occur in a group that are considered to have been entrapped at the same time (i.e., a fluid inclusion assemblage (FIA); Goldstein and Reynolds, 1994). The FIA include clusters, healed fractures (within a broad growth zone) and growth zones (Table 1). For isolated inclusions, those with vapor percentages obviously larger than the neighboring inclusions were considered heterogeneously entrapped and were not analyzed (Chi and Lu, 2008). For fluid inclusions in FIAs, variations of homogenization temperatures (T_h) up to 40 °C within individual FIAs were tolerated considering that many of the FIAs could only be loosely defined (i.e., the fluid inclusions within the FIA may not have been entrapped strictly at the same time). However, more than half of the FIAs have T_h variations less than 15 °C, which satisfies the criteria for good FIAs as suggested by Goldstein and Reynolds (1994). The average T_h and salinity values of individual FIAs are presented in Figs. 8–10. No systematic differences were observed between fluid inclusions from the two phases of quartz (Qz2 and Qz3), and their microthermometric attributes are described together as follows.

Many of the fluid inclusions did not freeze even after cooling to -185 °C, which is common for the H_2O -NaCl- $CaCl_2$ system (Chu et al., 2016). For those that were successfully frozen, the first melting temperature (T_m) values were generally below -60 °C (Table 1), also typical of the H_2O -NaCl- $CaCl_2$ system (Chi et al., 2014b; Chu et al., 2016).

Ice-melting temperatures (T_{m-ice}), and to a lesser extent, hydrohalite-melting temperatures (T_{m-HH}), were measured for many fluid inclusions (Table 1). In some cases, T_{m-HH} values are lower than T_{m-ice} , and the fluid composition falls in the field of final melting of ice (Fig. 8). In such cases, T_{m-HH} was used to calculate the X_{NaCl} value (i.e., NaCl/(NaCl + $CaCl_2$) ratio), as explained in Chi and Ni (2007) and Steele-MacInnis et al. (2011). In other cases, T_{m-ice} was measured and T_{m-HH} was not. In such cases, T_{m-ice} was used to estimate the maximum X_{NaCl} (Chi and Ni, 2007), and the fluid composition falls on the ice – hydrohalite cotectic curve with an arrow if T_{m-ice} is < -21.2 °C (Fig. 8; arrow indicates the direction of the actual composition of the fluid), or on the H_2O -NaCl binary if T_{m-ice} is > -21.2 °C (Fig. 8). Still in many other cases, T_{m-ice} is lower than T_{m-HH} , and the fluid composition should fall in the field of final melting of hydrohalite. In most of these cases, the T_{m-HH} value is higher than the hydrohalite stability field, suggesting metastable melting of hydrohalite (Bakker and Baumgartner, 2012). In such cases, we used the program of Steele-MacInnis et al. (2011) to calculate X_{NaCl} from T_{m-ice} and estimate the maximum possible T_{m-HH} for the measured T_{m-ice} , and the fluid composition thus plots on the hydrohalite – halite cotectic curve with an arrow (Fig. 8; arrow indicates the direction of the actual composition of the fluid).

The majority of T_{m-ice} values range from -39.7 to -23.4 °C, with one outlier at -51.5 °C and a few from -17.8 to -0.8 °C (Table 1). The low T_{m-ice} values (< -21.2 °C for the H_2O -NaCl system) are consistent with the H_2O -NaCl- $CaCl_2$ system, which has a eutectic point of -52 °C (Chi and Ni, 2007; Steele-MacInnis et al.,

Table 1
Microthermometric results of fluid inclusions from the Phoenix uranium deposit.*

FI ocr	Sz / μ	V%	Tfm / $^{\circ}$ C	Tm- HH / $^{\circ}$ C	Tm- ice / $^{\circ}$ C	Th / $^{\circ}$ C	Tm- H / $^{\circ}$ C	Sal /wt%	XNaCl
#14-KW-028I (DDH WR-328, 332.4 m), Qz2									
Cl	10	8	–	11.9	–29.3	148	–	27.6	0.40
	3	10	–	14.3	–36.4	123	–	29.1	0.21
	10	8	–80	8.7	–28.3	122	–	27.5	0.44
	2	10	–	–	–27.3	127	–	25.4	0.42
	3	8	–	–	–	137	–	–	–
	5	10	–	–	–	113	–	–	–
	4	10	–	–	–	119	–	–	–
	6	11	–	0.7	–27.1	134	–	27.2	0.50
#WR-13-35 (DDH WR-250, 341.8 m), Qz3									
Is	7	7	–	–	–	112	–	–	–
Is	16	7	–	–	–	123	–	–	–
Cl	10	7	–	–	–	114	–	–	–
	24	7	–57	–	–33.6	120	137	33.0	0.45
	6	7	–	–	–	115	–	–	–
	10	7	–	–	–	118	–	–	–
	14	7	–	–	–	120	–	–	–
	20	7	< –50	14.0	–25.2	134	–	26.9	0.62
Is	8	7	–	–	–	122	–	–	–
Is	26	7	–	–	–	101	–	–	–
Is	30	10	–	–	–	116	–	–	–
Is	7	10	–	–	–	122	–	–	–
Is	70	8	–	–	–	122	–	–	–
Is	18	8	–	–	–30.0	107	–	26.2	0.30
Is	24	7	–	–	–24.8	97	–	24.6	0.59
Is	14	13	–	–	–10.4	132	–	14.4	1.00
Is	14	10	–	–	–	82	–	–	–
#14-KW-27 (DDH WR-328, 369.8 m), Qz3									
Is	10	8	–	–	–0.8	90	–	1.2	1.00
Is	16	7	–	–	–	112	–	–	–
Is	8	8	–79	–35.0	–25.5	109	–	23.6	0.17
Is	10	8	–	–	–	135	–	–	–
Is	5	7	–	–	–	82	–	–	–
Is	16	7	–	–	–	113	–	–	–
Is	12	7	–79	–31.0	–26.4	94	–	24.4	0.27
Is	9	8	–	–	–	135	–	–	–
Is	10	7	–	–	–25.7	124	–	24.9	0.53
Is	10	8	–	–	–23.6	91	–	24.2	0.70
Is	12	8	–56	–25.7	–24.5	124	–	24.2	0.53
Is	12	5	–	–	–	80	–	–	–
Is	12	4	–	–	–	118	–	–	–
Is	8	11	–	–	–	123	–	–	–
Is	18	8	–	–	–	113	–	–	–
#14-KW-30 (DDH WR-328, 326.8 m), Qz3									
Cl	10	8	–	–	–	115	–	–	–
	7	10	–	–	–	109	–	–	–
	5	10	–	–	–	122	–	–	–
	14	8	–	–	–	117	–	–	–
	6	10	–	–	–	115	–	–	–
	6	8	–	–	–	115	–	–	–
	7	8	–	–	–	120	–	–	–
GZ	5	8	–	–	–	109	–	–	–
	20	8	–	–	–	118	–	–	–
	30	8	–	–	–	112	–	–	–
GZ	20	8	–	–	–	120	–	–	–
	10	8	–	–	–	117	–	–	–
	14	9	–	–	–	121	–	–	–
	5	9	–	–	–	127	–	–	–
	16	9	–	–	–	112	–	–	–
	8	8	–	–	–	114	–	–	–
Cl	5	11	–	–	–	131	–	–	–
	11	8	–	–	–	131	–	–	–
	22	10	–	7.0	–24.7	138	–	26.8	0.66
	9	10	–70	13.0	–25.0	133	–	26.9	0.64
	13	10	–65	15.0	–25.0	129	–	26.9	0.64
Cl	11	10	–70	12.4	–26.0	132	–	27.0	0.57
	10	11	–	–	–	131	–	–	–
	20	10	–70	13.5	–25.0	132	–	26.9	0.64
	10	9	–70	10.0	–25.0	130	–	26.9	0.64
	6	11	–	–	–	134	–	–	–

(continued on next page)

Table 1 (continued)

FI ocr	Sz /μ	V%	Tfm /°C	Tm- HH /°C	Tm- ice /°C	Th /°C	Tm- H /°C	Sal /wt%	XNaCL
GZ	10	9	–	–	–	120	–	–	–
	6	10	–	–	–	124	–	–	–
	15	10	–	–	–	132	–	–	–
	6	10	–	–	–	121	–	–	–
	9	10	–	–	–	118	–	–	–
GZ	5	10	–	–	–	117	–	–	–
	7	10	–	–	–	122	–	–	–
	12	10	–	–	–	132	–	–	–
GZ	12	10	–	–	–	127	–	–	–
	8	10	–	–	–	126	–	–	–
	6	10	–	–	–	127	–	–	–
	12	10	–	–	–	127	–	–	–
GZ	5	10	–	–	–	126	–	–	–
	7	10	–	–	–	131	–	–	–
	5	11	–	–	–	127	–	–	–
Is	12	10	–60	–8	–25.7	139	–	27.0	0.59
Is	14	9	–66	25	–25.6	157	–	27.0	0.59
GZ	10	8	–	–	–	117	–	–	–
	6	10	–	–	–	115	–	–	–
	12	8	–	–	–	119	–	–	–
	12	8	–	–	–	119	–	–	–
Is	8	8	–	–	–	122	–	–	–
Is	10	8	–	–	–	116	–	–	–
Is	20	8	–	–	–37.9	119	–	28.4	0.13
Is	16	8	–	4.8	–17.8	127	–	20.8	1.00
Cl	10	8	< –60	–	–29.1	115	–	26.0	0.34
	15	8	< –60	–	–28.5	107	–	25.8	0.36
	13	8	–	–	–	120	–	–	–
	5	8	–	–	–	108	–	–	–
	9	8	–	–	–	117	–	–	–
	13	8	–	–	–	118	–	–	–
GZ	4	9	–	–	–	113	–	–	–
	10	9	–	–	–	119	–	–	–
	12	9	–	–	–	106	–	–	–
	5	10	–	–	–	118	–	–	–
	13	8	–	–	–	117	–	–	–
	10	10	–	–	–	117	–	–	–
	20	9	–	–	–	124	–	–	–
	6	10	–	–	–	121	–	–	–
Cl	7	9	–	–	–	119	–	–	–
	14	10	–	–	–	117	–	–	–
	15	9	–	–	–	118	–	–	–
	5	10	–	–	–	115	–	–	–
	12	10	–	–	–	120	–	–	–
	11	9	–	–	–	117	–	–	–
#14-KW-028I (DDH WR-328, 332.4 m), Qz3									
GZ	6	10	–	–	–	122	–	–	–
	4	10	–	–	–	117	–	–	–
	20	9	–	7.5	–24.4	128	–	26.7	0.63
	5	9	–	–	–24.8	115	–	24.6	0.59
	12	9	–	–	–	121	–	–	–
GZ	8	8	–	–	–	124	–	–	–
	5	10	–	12.4	–24.0	129	–	26.7	0.71
	10	8	–	4.6	–24.9	101	–	26.8	0.64
	12	8	–	–	–	105	–	–	–
GZ	4	8	–	–	–	113	–	–	–
	14	8	–	–	–	110	–	–	–
GZ	8	8	–	–	–	115	–	–	–
	4	8	–	–	–	113	–	–	–
	6	8	–	–	–	120	–	–	–
	5	8	–	–	–	132	–	–	–
	4	8	–	–	–	122	–	–	–
Is	12	8	–	–	–	108	–	–	–
GZ	6	8	–	–	–	128	–	–	–
	5	8	–	–	–	112	–	–	–
GZ	10	8	–	–	–	122	–	–	–
	10	10	–	–	–	104	–	–	–
	9	8	–	–	–	128	–	–	–
	7	8	–	–	–	110	–	–	–
GZ	4	9	–	–	–	111	–	–	–
	8	8	–	–	–	112	–	–	–
	8	9	–	–	–	120	–	–	–

(continued on next page)

Table 1 (continued)

FI ocr	Sz /μ	V%	Tfm /°C	Tm- HH /°C	Tm- ice /°C	Th /°C	Tm- H /°C	Sal /wt%	XNaCl
GZ	14	10	–	–	–	115	–	–	–
	4	10	–	–	–	116	–	–	–
	10	8	–	–	–	114	–	–	–
	6	7	–	–	–	120	–	–	–
	8	8	–	–	–	108	–	–	–
	12	8	–	–	–	122	–	–	–
GZ	10	8	–	–	–	131	–	–	–
	12	9	–	–	–	120	–	–	–
	5	10	–	–	–	130	–	–	–
	16	10	–58	16.8	–25.4	140	–	26.9	0.61
	7	7	–	–5.1	–25.1	131	–	26.8	0.63
GZ	5	10	–	–	–	121	–	–	–
	10	10	–	–	–	112	–	–	–
	5	10	–	–	–	100	–	–	–
	7	10	–	–	–	117	–	–	–
	10	9	–	11.3	–33.6	107	–	28.4	0.26
HF	8	8	–	–	–	142	–	–	–
	3	9	–	–	–	128	–	–	–
	8	8	–	–	–	128	–	–	–
	6	9	–	–	–	132	–	–	–
	5	8	–	–	–	120	–	–	–
	3	10	–	–	–	118	–	–	–
HF	18	8	–60	13.7	–24.5	147	–	26.7	0.67
	3	10	–	–	–23.4	124	–	24.1	0.72
	4	10	–	–	–23.4	118	–	24.1	0.72
	10	11	–	–	–	136	–	–	–
	7	10	–	–	–25.8	116	–	24.9	0.52
	5	9	–	–	–24.9	126	–	24.6	0.59
GZ	9	10	–	–	–	115	–	–	–
	5	8	–	–	–	108	–	–	–
	8	9	–	–	–	108	–	–	–
Cl	6	10	–	–	–37.6	128	–	28.3	0.14
	18	8	–70	–	–27.2	123	–	25.4	0.43
	9	10	–	–	–	122	–	–	–
	6	10	–	–	–	107	–	–	–
	6	15	–	–	–28.3	139	–	25.7	0.37
	13	8	–70	9.8	–27.4	127	–	27.3	0.49
HF	8	8	–	–	–	120	–	–	–
	6	10	–	–	–	117	–	–	–
	7	8	–	–	–	131	–	–	–
	4	10	–	–	–	98	–	–	–
	3	7	–	–	–	94	–	–	–
	6	11	–	–	–	116	–	–	–
GZ	7	10	–	–	–	139	–	–	–
	4	6	–	–	–	99	–	–	–
	5	9	–	–	–	111	–	–	–
	7	10	–	–	–	129	–	–	–
GZ	7	10	–	–	–	139	–	–	–
	5	11	–	–	–	129	–	–	–
	10	9	–	–	–	139	–	–	–
	6	9	–	–	–	139	–	–	–
	4	9	–	–	–	136	–	–	–
HF	28	8	–	–	–	126	–	–	–
	14	8	–	–	–	119	–	–	–
	24	7	–	–	–	105	–	–	–
	12	7	–70	5.7	–26.8	115	–	27.2	0.52
	6	9	–	4.5	–25.3	96	–	27.2	0.62
	9	9	–63	–2.1	–24.9	129	–	26.8	0.64
	6	8	–	–	–	136	–	–	–
GZ	12	7	–	–	–	102	–	–	–
	12	8	–	–	–	108	–	–	–
	14	8	–57	–	–25.3	124	–	24.8	0.55
GZ	10	8	–	8.6	–25.2	118	–	26.9	0.62
	12	7	–	–	–	111	–	–	–
	4	10	–	–	–	114	–	–	–
	5	11	< –60	–1.3	–25.3	128	–	26.9	0.61
	7	10	–73	–	–25.1	129	–	24.7	0.57
	16	10	–	–	–	120	–	–	–

(continued on next page)

Table 1 (continued)

FI ocr	Sz /μ	V%	Tfm /°C	Tm- HH /°C	Tm- ice /°C	Th /°C	Tm- H /°C	Sal /wt%	XNaCL
GZ	10	7	–	–	–	129	–	–	–
	30	8	< –65	8.9	–25.6	118	–	27.0	0.59
	5	10	–	–	–	127	–	–	–
	12	8	–	11.2	–24.4	117	–	26.7	0.63
	7	8	–73	13.6	–24.6	119	–	26.7	0.67
	10	7	–	–	–	108	–	–	–
	7	9	–	7.5	–25.7	118	–	27.0	0.59
	3	9	–	–	–24.5	110	–	24.5	0.62
	10	7	–	–	–25.4	119	–	24.8	0.55
GZ	10	7	–60	12.7	–25.7	121	–	27.0	0.59
	12	7	–	–	–	103	–	–	–
	6	10	–	–	–	126	–	–	–
GZ	13	8	–	–	–	111	–	–	–
	12	7	–	–	–	121	–	–	–
	15	7	–	–	–	108	–	–	–
	8	9	< –60	–9.1	–26.4	115	–	27.1	0.54
	8	8	–	–	–	121	–	–	–
GZ	5	10	–	–	–	133	–	–	–
	2	12	–	–	–	136	–	–	–
	4	9	–	–	–	141	–	–	–
	8	8	–	–	–	120	–	–	–
	8	7	–	–	–	122	–	–	–
	9	10	–	–	–	136	–	–	–
GZ	7	9	–70	–	–35.0	118	–	27.7	0.17
	10	7	–	–	–	120	–	–	–
	8	8	–	–	–	121	–	–	–
	2	10	–	–	–	115	–	–	–
	2	10	–	–	–	118	–	–	–
GZ	4	12	–	–	–	108	–	–	–
	5	11	–	–	–	121	–	–	–
	7	8	–	–	–	122	–	–	–
	3	11	–	–	–	117	–	–	–
	4	12	–	–	–	122	–	–	–
	3	10	–	–	–	115	–	–	–
	10	9	–70	–	–34.1	129	–	27.4	0.19
GZ	6	10	–	–	–26.4	130	–	25.1	0.48
	6	10	–	–	–	112	–	–	–
	3	10	–	–	–	114	–	–	–
GZ	8	8	–	–	–	112	–	–	–
	9	10	–	–	–	134	–	–	–
	8	9	–	–	–	116	–	–	–
	7	10	–	–	–	114	–	–	–
GZ	3	10	–	–	–	108	–	–	–
	7	10	–	–	–	117	–	–	–
	9	9	–	–	–	129	–	–	–
	7	10	–	–	–	119	–	–	–
GZ	11	9	–	–	–	132	–	–	–
	10	10	–	–	–	120	–	–	–
GZ	9	11	–	–	–	128	–	–	–
	6	10	–	–	–	106	–	–	–
GZ	14	8	–	–	–	109	–	–	–
	8	10	–	–	–	121	–	–	–
	7	8	–	–	–	110	–	–	–
	13	8	–	–	–	142	–	–	–
	9	9	–	–	–	106	–	–	–
GZ	9	9	–	–	–	115	–	–	–
	14	8	–	–	–	140	–	–	–
	8	9	–	–	–	114	–	–	–
	7	10	–	–	–	102	–	–	–
	9	10	–	–	–	122	–	–	–
	6	10	–	–	–	122	–	–	–
	16	10	–	–	–	111	–	–	–
#14-KW-028II (DDH WR-328, 332.4 m), Qz3									
GZ	6	10	–	7.3	–26.5	113	–	27.1	0.54
	7	7	–	–	–	109	–	–	–
	7	11	–58	6.8	–27.3	123	–	27.3	0.49
Cl	10	10	–	–	–0.9	105	–	1.4	1.00
	12	8	–	–	–	102	–	–	–

(continued on next page)

Table 1 (continued)

FI ocr	Sz /μ	V%	Tfm /°C	Tm- HH /°C	Tm- ice /°C	Th /°C	Tm- H /°C	Sal /wt%	XNaCL
GZ	13	10	−70	−	−28.1	123	−	25.7	0.38
	8	10	−	−	−	124	−	−	−
	5	10	−	−28.9	−26.8	114	−	24.8	0.35
	11	10	−	−	−	131	−	−	−
	15	11	−70	5.5	−26.7	118	−	27.2	0.52
	19	9	−72	6.7	−27.2	116	−	27.3	0.50
	5	12	−	−49.4	−28.7	149	−	24.6	0.06
	20	8	−80	6.0	−25.7	107	−	27.0	0.59
GZ	8	10	−	−	−	106	−	−	−
	6	10	−	−	−	121	−	−	−
	11	11	−77	8.4	−28.3	119	−	27.5	0.44
	6	10	−	−	−	112	−	−	−
Is	7	9	−63	−43.1	−25.6	124	−	23.4	0.09
HF	5	10	−	−	−	101	−	−	−
	4	13	−	−	−	130	−	−	−
	2	10	−	−	−	104	−	−	−
	3	10	−	−	−	103	−	−	−
	6	8	−	−	−	97	−	−	−
	6	10	−	−	−	124	−	−	−
	5	9	−	−	−	104	−	−	−
	8	10	−	−	−	119	−	−	−
	4	12	−	−	−	105	−	−	−
Cl	18	8	−	−	−	108	−	−	−
	6	10	−	−	−26.2	118	−	25.1	0.49
	9	8	−	−	−	100	−	−	−
Is	10	10	−	−	−	111	−	−	−
Is	10	8	−	−	−	151	−	−	−
#14-KW-032 (DDH WR-328, 304.1 m), Qz3									
HF	10	10	−	−	−24.9	117	−	24.6	0.59
	8	10	−	5.9	−24.9	125	−	26.8	0.64
	6	10	−	−	−24.7	125	−	24.6	0.60
	8	11	−60	−	−25.0	132	−	24.7	0.58
	18	10	−	−	−	130	−	−	−
	12	10	−65	−	−26.8	124	−	25.2	0.45
	8	9	−	−	−25.2	126	−	24.7	0.56
	5	10	−	−	−	126	−	−	−
	9	12	< −70	−	−26.8	129	−	25.2	0.45
	5	11	−	−	−	127	−	−	−
HF	8	8	−67	3.2	−25.2	130	−	26.9	0.62
	9	10	−63	−	−24.6	134	−	24.5	0.61
	18	10	−65	13.7	−24.0	122	−	26.7	0.71
	11	9	−63	−	−27.7	129	−	25.5	0.40
	8	8	−	−	−	108	−	−	−
	14	10	−	−	−	134	−	−	−
	11	9	−	−	−	136	−	−	−
	7	10	−	−	−	117	−	−	−
Is	10	10	−	−	−	115	−	−	−
GZ	10	9	−	−	−	109	−	−	−
	10	10	−74	−	−27.1	133	−	25.3	0.44
	12	8	−	−	−	116	−	−	−
GZ	10	10	−75	6.5	−27.9	116	−	27.4	0.46
	6	10	−	−	−	114	−	−	−
	10	9	−	−	−	119	−	−	−
GZ	5	9	−	−	−	115	−	−	−
	6	9	−73	7.3	−26.9	135	−	27.2	0.51
	4	10	−	−	−	134	−	−	−
GZ	6	10	< −77	−	−28.4	133	−	25.7	0.37
	6	10	< −75	−0.1	−27.4	138	−	27.3	0.49
	4	10	−	−	−	120	−	−	−
	7	10	−	−	−	122	−	−	−
	11	9	−	−	−	120	−	−	−
GZ	22	8	−	−	−	124	−	−	−
	14	9	−82	−51.7	−51.5	128	−	31.3	0.06
	5	10	−	−	−	119	−	−	−
GZ	10	10	−80	13.5	−31.7	124	−	29.0	0.31
	10	10	−	−	−	123	−	−	−
	3	10	−	−	−	113	−	−	−
	8	9	−78	6.9	−27.5	125	−	27.3	0.48
	10	10	−	−	−	122	−	−	−
GZ	12	9	< −84	−	−32.0	119	146	32.9	0.49
	4	8	−	−	−	122	−	−	−
	5	10	−	−	−	121	−	−	−
	20	8	−87	−	−29.1	130	160	32.5	0.57

(continued on next page)

Table 1 (continued)

FI ocr	Sz /μ	V%	T _{fm} /°C	T _m -HH /°C	T _m -ice /°C	T _h /°C	T _m -H /°C	Sal /wt%	X _{NaCl}
GZ	10	10	–	–	–	125	–	–	–
	7	10	–	–	–	122	–	–	–
	8	8	–	–	–	121	–	–	–
	5	10	–	–	–	121	–	–	–
HF	8	9	–	–	–	115	–	–	–
	16	8	–	–	–	119	–	–	–
	9	9	–	–	–	118	–	–	–
	6	8	–	–	–	126	–	–	–

* Is – isolated; Cl – cluster; GZ – growth zone; HF – healed fracture; FIA – Fluid Inclusion Assemblage; Ocr – occurrence; Sz – size; V % – vapor percentage; T_{fm} – first-melting temperature; T_m-HH – hydrohalite-melting temperature; T_m-ice – ice-melting temperature; T_h – homogenization (vapor to liquid) temperature; T_m-H – halite dissolution temperature; Sal – salinity; X_{NaCl} – NaCl/(NaCl + CaCl₂) weight ratio; “–” – data unavailable (fluid inclusion did not freeze or melting was uncertain); *italics* – metastable measurements

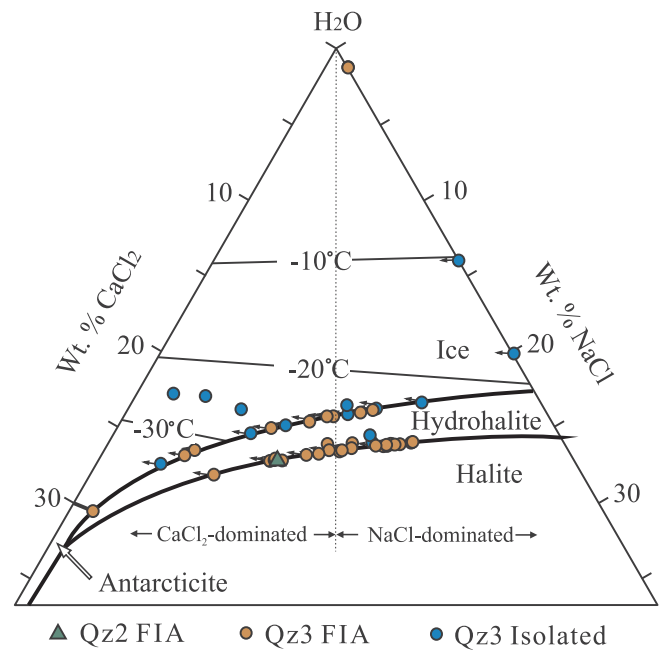


Fig. 8. A H₂O-NaCl-CaCl₂ phase diagram showing the stability fields of ice, hydrohalite, halite and antarctite, and the composition of the fluid inclusions analyzed in this study. The fluid composition plotted is based on the microthermometric data using the program by Steele-MacInnis et al. (2011). The arrows indicate the direction of the position of the fluid composition (see text for discussion).

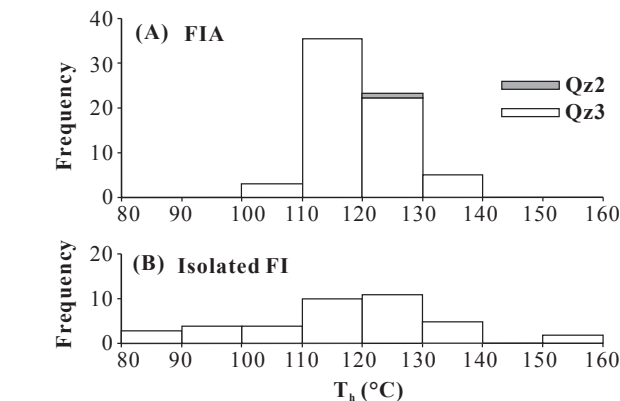


Fig. 9. Histograms of homogenization temperatures for biphasic fluid inclusions from (A) Qz2 and Qz3 fluid inclusion assemblages and (B) isolated fluid inclusions. Note the averages of individual FIAs, rather than the T_h values of individual fluid inclusions, were used in the making of the histogram in A.

2011). The T_m-HH values range from −51.7 to +25 °C (Table 1), most of which are metastable (i.e., higher than temperatures expected for the stability field of hydrohalite). The combination of T_m-ice and maximum stable T_m-HH values yield fluid salinities from 20.8 to 33.0 wt% (with three outliers at 1.2, 1.4 and 14.4 wt%), and maximum X_{NaCl} values from 0.06 to 0.72 (with a few outliers at 1.0), indicating that the fluids range from NaCl-dominated to CaCl₂-dominated brines (Fig. 8). T_h values range from 80 to 157 °C, with a relatively tight cluster from 104 to 132 °C for FIAs in Qz3 (only one FIA with an average T_h of 128 °C in Qz2) compared to the relatively wide spread of T_h values for isolated fluid inclusions (Fig. 9). In the T_h – salinity diagram (Fig. 10), the spread of T_h values is in contrast with the relatively narrow range of salinity (one single value of 27.4 wt% for a FIA in Qz2, 24.8–31.1 wt% for FIAs in Qz3, and 20.8–28.4 wt% for isolated fluid inclusions in Qz3 with few outliers ≤14.4 wt%). The three triphase inclusions measured have vapor disappearance temperatures from 119 to 130 °C and halite melting temperatures from 137 to 160 °C, which yielded salinities from 32.5 to 33.0 wt% (Table 1). As these inclusions are interpreted to have resulted from heterogeneous trapping, their microthermometric data were not used.

5.3. Cryogenic Raman spectroscopic study of solute composition

Cryogenic Raman spectroscopic analysis of fluid inclusions from Qz3 (Fig. 11) show three different types of spectra suggesting three solutions: NaCl-dominated H₂O-NaCl-CaCl₂, CaCl₂-dominated H₂O-NaCl-CaCl₂, and MgCl₂-NaCl-CaCl₂-H₂O. The NaCl-dominated H₂O-NaCl-CaCl₂ solution is characterized by prominent peaks at 3404–3406, 3422–3423, 3436–3438 and 3536–3539 cm^{−1} (Fig. 11A). The CaCl₂-dominated H₂O-NaCl-CaCl₂ solution (Fig. 11B) has similar Raman peaks as the NaCl-dominated one, but with an additional minor shoulder at ~3386 cm^{−1} and a minor peak at 3462–3467 cm^{−1}

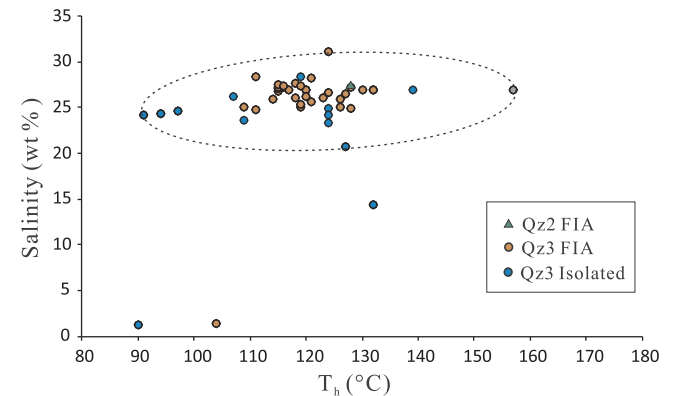


Fig. 10. Salinity-homogenization temperature diagram of biphasic fluid inclusions from Qz2 and Qz3.

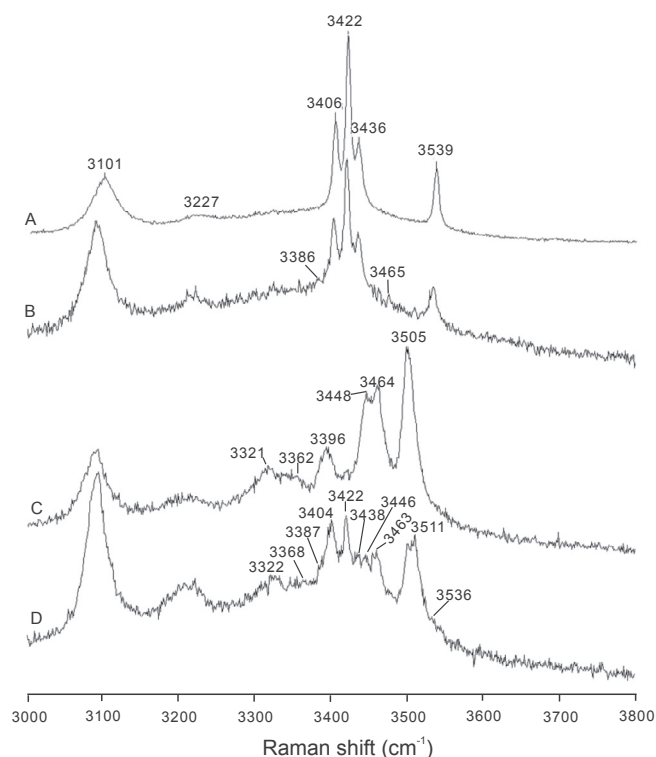


Fig. 11. Raman spectra of fluid inclusions showing various hydrates at $-185\text{ }^{\circ}\text{C}$ (see text for the meaning of individual peaks) from Qz3 in sample 14-KW-032. Spectrum A is typical of NaCl-dominated fluid; spectrum B indicates presence of CaCl_2 ; spectra C and D indicate presence of MgCl_2 in addition to NaCl and CaCl_2 .

(Fig. 11B), which may be attributed to antarcticite ($\text{CaCl}_2 \cdot 6\text{H}_2\text{O}$) and sinjarite ($\text{CaCl}_2 \cdot 2\text{H}_2\text{O}$) \pm γ -tetrahydrate ($\gamma\text{-CaCl}_2 \cdot 4\text{H}_2\text{O}$) (Baumgartner and Bakker, 2009, 2010; Chi et al., 2014b). In addition, the peak at 3539 cm^{-1} is lower than that for the NaCl-dominated solution (Fig. 11A). The MgCl_2 -bearing fluid inclusions show multiple peaks at $3320\text{--}3322\text{ cm}^{-1}$, 3368 cm^{-1} , $3446\text{--}3448\text{ cm}^{-1}$, and $3505\text{--}3513\text{ cm}^{-1}$ (Fig. 11C and D). The peaks at $3320\text{--}3322\text{ cm}^{-1}$ and $3505\text{--}3513\text{ cm}^{-1}$ may be attributed to $\text{MgCl}_2 \cdot 12\text{H}_2\text{O}$ (Baumgartner and Bakker, 2009, 2010) and the peak at $3446\text{--}3448\text{ cm}^{-1}$ is likely caused by $\alpha\text{-CaCl}_2 \cdot 4\text{H}_2\text{O}$ (Baumgartner and Bakker, 2009).

5.4. Volatile compositions of fluid inclusions

Nine samples, including one sample of Qz2 and eight samples of Qz3, were analyzed for the volatile compositions of bulk fluid inclusions. Because the fluid inclusions in the drusy quartz are of the four types described above regardless the occurrences, the bulk fluid inclusions are believed to represent the mineralizing fluids. Four to ten successive batches of gas components were released from each sample depending on the amount and the size of the quartz grains. H_2O , CO_2 , CH_4 , N_2 , H_2 , O_2 , He and Ar were detected, with concentrations comparable amongst different batches within individual samples (Table 2).

H_2O is $\geq 99\text{ mol}\%$ in all the samples analyzed, with non-aqueous volatiles comprising $\leq 1\text{ mol}\%$ (Table 1). The average contents (mol%) of volatiles of fluid inclusions in Qz2 are: 99.51 for H_2O , 0.094 for CO_2 , 0.0137 for CH_4 , 0.34 for N_2 , 0.0238 for H_2 , 0.008 for O_2 , 0.001 for He and 0.0052 for Ar. The average contents (mol%) of volatiles of fluid inclusions in Qz3 are: 99.0–99.84 for H_2O , 0.013–0.032 for CO_2 , 0.0025–0.0064 for CH_4 , 0.1–0.81 for N_2 , 0.0001–0.0244 for H_2 , 0.026–0.148 for O_2 , 0.0001–0.0005 for He and 0.0018–0.0124 for Ar. Thus, there is no significant difference in the content of various volatile species measured between Qz2 and Qz3.

When the data are plotted on the CO_2/N_2 – Total volatile (non-aqueous) content diagram (Fig. 12; Blamey, 2012), they show a trend that is expected for fluids experiencing boiling. Such a trend, called the “boiling slope” in Blamey (2012), is particularly well developed for Qz3, which is consistent with the widespread development of vapor-only and vapor-dominated fluid inclusions suggesting fluid boiling as discussed above. The data from Qz2, although limited in number, also broadly fall on the same trend, which is consistent with the observation of fluid inclusion assemblages indicative boiling in this phase of quartz as well (Fig. 7C and D).

5.5. Fluid pressure calculation

The coexistence of liquid-dominated and vapor-dominated biphasic, vapor-only monophasic, and halite-bearing triphasic aqueous fluid inclusions within individual FIAs indicates that both liquid and vapor phases were present during the precipitation of Qz2 and Qz3, i.e., fluid immiscibility or boiling. Because the fluids have low concentrations of non-aqueous volatiles ($< 1\text{ mol}\%$) as discussed above, it is more appropriate to call this phenomenon “boiling” rather than “fluid immiscibility”. For homogeneously entrapped fluid inclusions from a boiling system, the homogenization temperature represents the actual trapping temperature, and the pressure (P_{H}) at these temperatures represents the trapping pressure.

A few fluid inclusions within the main range in the T_{H} – salinity diagram (Fig. 10) were selected for calculation of P_{H} and the results are shown in Table 3. Assuming a H_2O –NaCl system, the calculated P_{H} values range from 5 to 6 bars for a T_{H} range from 91 to $157\text{ }^{\circ}\text{C}$ (Table 3). These fluid pressures are likely underestimated, as the influence of non-aqueous volatiles was not taken into consideration. However, such influence is likely to be small because the concentrations of the non-aqueous volatiles are low. Assuming a H_2O – CO_2 system with CO_2 concentrations of 1 mol% and 2 mol%, the calculated P_{H} values range from 3 to 11 bars and from 5 to 17 bars, respectively (Table 3). The significance of these low fluid pressures will be discussed in the next section.

6. Discussion

Petrographic and fluid inclusion studies have revealed that the Phoenix uranium deposit formed from H_2O –NaCl– $\text{CaCl}_2 \pm \text{MgCl}_2$ brines, likely derived from within the Athabasca Basin, at temperatures from 90 to $157\text{ }^{\circ}\text{C}$. This inference is in general agreement with the “diagenetic-hydrothermal” model that has been widely accepted for the unconformity-related uranium deposits (Hoeve and Sibbald, 1978; Pagel et al., 1980; Hoeve and Quirt, 1984; Wilde et al., 1989; Kotzer and Kyser, 1995; Derome et al., 2005; Polito et al., 2005; Richard et al., 2016). However, the recognition of fluid boiling, and the related relatively low fluid temperatures and pressures, imply a significantly different mineralization environment and process from those invoked in the conventional model. The significance of this study for the genesis of the Phoenix uranium deposit is further discussed below in terms of depth of mineralization, fluid-flow driving forces and ore precipitation mechanisms.

The relatively low fluid inclusion homogenization temperatures ($90\text{--}157\text{ }^{\circ}\text{C}$; Figs. 9 and 10) are significantly lower than the burial temperatures of $\sim 200\text{ }^{\circ}\text{C}$ or more as estimated in the conventional “diagenetic-hydrothermal” model (Pagel, 1975; Kotzer and Kyser, 1995; Derome et al., 2005). These elevated burial temperatures are mainly based on three techniques, i.e., clay mineral thermometry (e.g. Hoeve and Quirt, 1984; Alexandre et al., 2005), oxygen isotope thermometry (e.g. Kotzer and Kyser, 1995), and the intersection of fluid inclusion isochores with geothermal gradients (e.g. Derome et al., 2005; Richard et al., 2016). While these temperatures may reflect the maximum temperatures of the hydrothermal fluids, they may not be used to estimate the burial depths based on normal geothermal gradients. If the

Table 2

Volatile compositions of bulk fluid inclusions in hydrothermal quartz from the Phoenix deposit (mol %).

Sample #	Batches	H ₂ O	CO ₂	CH ₄	N ₂	H ₂	O ₂	He	Ar
14-KW-007 (DDH WR-328, 348.1 m), Qz2									
	9456b	99.71	0.084	0.0128	0.15	0.0277	0.01	0	0.0025
	9456c	99.93	0.013	0.0019	0.04	0.0066	0.006	0.0001	0.0005
	9456d	99.6	0.047	0.0073	0.32	0.0152	0.003	0.0001	0.0039
	9456e	99.14	0.207	0.0292	0.56	0.0431	0.016	0.0002	0.0101
Weighted Mean		99.51	0.094	0.0137	0.34	0.0238	0.008	0.0001	0.0052
WR-13-027 (DDH ZQ-20, 185.1 m, Qz3)									
	9453a	99.78	0.024	0.0022	0.16	0.0005	0.033	0.0008	0.0024
	9453b	99.86	0.016	0.0019	0.1	0	0.024	0.0003	0.0017
	9453c	99.81	0.024	0.0021	0.12	0	0.036	0	0.0021
	9453d	99.82	0.027	0.0025	0.11	0	0.04	0.0001	0.0022
	9453e	99.91	0.015	0.0019	0.06	0	0.017	0	0.0008
	9453f	99.84	0.024	0.0032	0.1	0	0.031	0.0001	0.0018
	9453 g	99.88	0.02	0.0026	0.07	0	0.025	0	0.0012
	9453 h	99.89	0.02	0.004	0.07	0.0002	0.017	0	0.0011
Weighted Mean		99.84	0.023	0.0025	0.1	0.0001	0.031	0.0002	0.0018
WR-13-035 (DDH WR-250, 341.8 m), Qz3									
	9460a	99.7	0.015	0.0024	0.24	0	0.039	0.0001	0.003
	9460b	99.81	0.049	0.0018	0.11	0.0006	0.019	0.0001	0.0014
	9460c	99.79	0.007	0.0016	0.17	0	0.029	0.0001	0.0021
	9460d	99.86	0.012	0.0024	0.1	0.0003	0.021	0	0.0016
	9460e	99.84	0.01	0.0034	0.12	0	0.025	0	0.0015
	9460f	99.76	0.021	0.0034	0.18	0.0003	0.038	0	0.0026
	9460 g	99.87	0.02	0.0028	0.09	0.0014	0.019	0.0001	0.0012
	9460 h	99.83	0.027	0.0044	0.12	0.0026	0.022	0.0001	0.0016
	9460j	99.87	0.019	0.0041	0.09	0.0033	0.012	0.0001	0.0011
Weighted Mean		99.81	0.017	0.0029	0.14	0.0007	0.026	0.0001	0.0019
14-KW-004 (DDH WR-328, 341.4 m), Qz3									
	9451c	99.53	0.028	0.005	0.38	0.0012	0.05	0.0004	0.0058
	9451d	98.98	0.043	0.0052	0.85	0.0146	0.101	0.0004	0.011
	9451e	99.48	0.028	0.0065	0.43	0.0104	0.04	0.0005	0.0055
	9451f	99.37	0.033	0.0067	0.52	0.0137	0.042	0.0008	0.0064
	9451 g	99.63	0.031	0.0032	0.3	0.0098	0.023	0.0004	0.0045
	9451 h	99.25	0.033	0.0087	0.62	0.0174	0.062	0.0006	0.008
	9451j	99.64	0.028	0.0069	0.28	0.0111	0.028	0.0003	0.0043
	9451 k	99.69	0.032	0.0089	0.23	0.0114	0.019	0.0002	0.0038
Weighted Mean		99.43	0.032	0.0064	0.46	0.011	0.047	0.0005	0.0063
14-KW-027 (DDH WR-328, 369.8 m), Qz3									
	9459a	99.32	0.012	0.0013	0.55	0.0168	0.088	0.0003	0.0069
	9459b	99.56	0.011	0.0049	0.36	0.0346	0.03	0.0003	0.0042
	9459c	99.74	0.014	0.0024	0.21	0.0175	0.017	0.0003	0.003
	9459d	99.83	0.018	0.0063	0.1	0.0363	0.007	0.0002	0.0013
Weighted Mean		99.55	0.013	0.0032	0.36	0.0244	0.045	0.0003	0.0045
14-KW-028 (DDH WR-328, 332.4 m), Qz3									
	9458a	99.64	0.018	0.0051	0.31	0.0015	0.022	0.0005	0.0038
	9458b	99.46	0.011	0.0044	0.44	0	0.079	0.0001	0.0066
	9458c	99.47	0.012	0.0029	0.45	0.0069	0.054	0.0005	0.0057
	9458d	99.56	0.017	0.007	0.34	0.021	0.05	0.0003	0.0053
	9458e	99.53	0.021	0.0184	0.35	0.0427	0.036	0.0003	0.0046
Weighted Mean		99.52	0.015	0.0062	0.39	0.0103	0.052	0.0003	0.0054
14-KW-030 (DDH WR-328, 326.8 m), Qz3									
	9454a	99.86	0.073	0.0008	0.05	0.0122	0.003	0.0003	0.0005
	9454b	99.54	0.026	0.0024	0.36	0	0.068	0	0.0058
	9454c	99.57	0.027	0.0026	0.36	0.0038	0.031	0.0001	0.0048
	9454d	99.7	0.01	0.0014	0.23	0	0.048	0.0001	0.0036
	9454e	99.69	0.013	0.0013	0.24	0.0017	0.05	0.0001	0.0037
	9454f	99.65	0.011	0.0028	0.29	0.0063	0.035	0.0008	0.0034
	9454 g	99.49	0.015	0.0042	0.43	0.0039	0.049	0.0001	0.0051
	9454 h	99.7	0.015	0.0028	0.23	0.0063	0.04	0.0005	0.0035
	9454j	99.85	0.021	0.0028	0.1	0.0075	0.01	0.0001	0.0016
	9454 k	99.8	0.016	0.0043	0.14	0.014	0.022	0.0001	0.0021
Weighted Mean		99.65	0.017	0.0028	0.28	0.0047	0.042	0.0002	0.0039
14-KW-032 (DDH WR-328, 304.1 m), Qz3									
	9455a	97.6	0.037	0.0074	1.95	0.0065	0.372	0.0001	0.0296
	9455b	99.01	0.017	0.0084	0.85	0.0094	0.102	0.0003	0.0102
	9455c	98.58	0.02	0.0035	1.13	0.0052	0.246	0.0001	0.0177
	9455d	98.92	0.013	0.0039	0.89	0.0017	0.164	0.0001	0.0126
	9455e	98.71	0.029	0.0056	1.03	0.0059	0.2	0.0002	0.0167
	9455f	99.53	0.015	0.0041	0.38	0.0014	0.069	0.0001	0.0064
	9455 g	99.49	0.02	0.0058	0.41	0.0083	0.059	0.0001	0.0062
	9455 h	99.33	0.031	0.0118	0.54	0.018	0.058	0.0002	0.0073

(continued on next page)

Table 2 (continued)

Sample #	Batches	H ₂ O	CO ₂	CH ₄	N ₂	H ₂	O ₂	He	Ar
Weighted Mean		99	0.022	0.0058	0.81	0.0065	0.148	0.0001	0.0124
14-KW-045 (DDH WR-267, 342.8 m), Qz3									
	9457a	99.76	0.016	0.0019	0.17	0	0.045	0.0003	0.003
	9457b	99.75	0.017	0.0057	0.18	0.0186	0.026	0.0005	0.0026
	9457c	99.8	0.018	0.0034	0.14	0	0.032	0.0001	0.0024
	9457d	99.85	0.016	0.0023	0.11	0.0022	0.018	0.0001	0.0018
	9457e	99.87	0.018	0.005	0.09	0	0.016	0.0001	0.0014
	9457f	99.79	0.017	0.0152	0.13	0.0296	0.017	0.0001	0.002
Weighted Mean		99.79	0.017	0.0042	0.15	0.0051	0.031	0.0002	0.0024

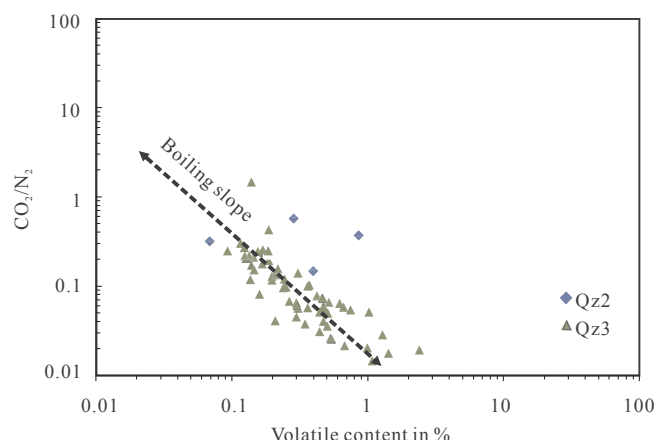


Fig. 12. A diagram showing a negative linear correlation between CO_2/N_2 ratios and total volatile (non-aqueous) contents (bulk fluid inclusion analysis) indicating fluid boiling (Blamey, 2012).

Table 3

Fluid pressure (P_h) at homogenization temperature (T_h) for fluid inclusions assuming different concentrations of CO_2 .

T_h (°C)	Salinity (wt %)	P_h (bar) (H_2O -NaCl system)	P_h (bar) (H_2O - CO_2 system)	
		$\text{CO}_2 = 0$ (mol%)	$\text{CO}_2 = 1$ (mol%)	$\text{CO}_2 = 2$ (mol%)
91	24.2	6	3	5
107	26.2	5	4	7
123	32.7	5	6	10
127	20.8	5	6	10
139	26.7	5	8	13
157	26.2	5	11	17

local geothermal gradient related to the hydrothermal system is significantly higher than the normal value (e.g., 70 °C/km rather than 35 °C/km), the depth of mineralization may be much shallower than implied in the conventional model (> 5 km). In fact, based on regional stratigraphy (Ramaekers et al., 2007), the thickness of the strata from the basal unconformity to the top of the Carswell Formation, which corresponds to the time of basinal brine formation and regional uranium mineralization (see Chi et al., 2018 for discussion), is around 1.5 km at the location of the Phoenix deposit. Applying a maximum decompaction factor of 1.7, as advocated by Chi et al. (2013), the depth of mineralization was possibly around 2.5 km (Chi et al., 2018). At a geothermal gradient of 35 °C/km (the standard used in the conventional model), the ambient temperature at a depth of 2.5 km would be around 108 °C (assuming a surface temperature of 20 °C). Thus, the variation of fluid temperatures from ~90 to ~160 °C documented in the Phoenix deposit could reflect temperature fluctuation between the ambient

(burial) and hydrothermal conditions in a shallow environment, as has been proposed for unconformity-related uranium deposits in general (Chi and Chu, 2016) and for the Athabasca Basin in particular (Chi et al., 2018). Similar ranges of fluid inclusion homogenization temperatures have also been reported in other studies of unconformity-related uranium deposits (Derome et al., 2005; Richard et al., 2016). The differences between this study and the previous studies are that we interpret the lower end of the homogenization temperature range to represent the ambient temperatures at shallow burial, whereas the previous studies derived higher fluid temperatures from the intersection of the isochores with “normal” geothermal gradients. In other words, in our model, the ore-forming fluids were hotter than the ambience, whereas in the conventional model, the ore-forming fluids were of more or less the same temperature as the ambience.

However, the extremely low fluid pressures estimated from fluid inclusions at boiling conditions (< 17 bars, Table 3) still cannot be adequately explained by the shallow (2.5 km) burial environment, which implies an ambient fluid pressure of about 250 bars (assuming a hydrostatic pressure regime). The low fluid pressures and associated fluid boiling are thus possibly related to an abrupt fluid pressure drop and “flash vaporization” (Weatherley and Henley, 2013) during fracturing in relation to post-Athabasca reactivation of the WS shear zone in the basement. The pressure gradient between the ambient hydrostatic pressure and the sub-hydrostatic pressure in the instantly opened fractures, as depicted in the seismic pumping model (Sibson, 1987; Sibson et al., 1988), may have been an important driving force of fluid flow related to the uranium mineralization. It should be pointed out, however, that although fluid inclusion assemblages commonly indicate fluid boiling, it does not mean that the fluid was boiling during the whole period of hydrothermal quartz precipitation. Instead, fluid boiling likely took place episodically and briefly in relation to repeated pressure releases during reactivation of the basement faults. Between individual faulting events, the fluid pressure may have returned to the normal hydrostatic regime, ending the boiling process. The re-establishment of ambient fluid pressures during the inter-faulting period may have converted the vapor phase that was produced during fluid boiling into a liquid phase (via condensation), which may explain the presence of the low-salinity fluid inclusions (Fig. 10). It is thus possible that fluid boiling only occupied a small part of the time during the precipitation of the hydrothermal quartz; the fluid was in the liquid status most of the time. Furthermore, although we propose that seismic pumping was an important driving force for fluid flow in the formation of the Phoenix deposit, fluid flow was active before and after seismic activity, and could have been driven by either thermal convection (Li et al., 2016) or compressional deformation (Li et al., 2017). In particular, egress (upward from basement to basin) fluid flow associated with reverse movement of the WS shear zone was predicted by numerical modeling (Li et al., 2018), consistent with the positioning of the deposit in relation to the fault and alteration pattern (Li et al., 2018).

In addition to providing constraints on fluid P-T conditions and fluid flow driving forces, fluid boiling has also been commonly considered as a critical ore deposition mechanism for some high crustal level mineral

deposits such as porphyry-copper and epithermal-gold deposits (Roedder, 1984; Roedder and Bodnar, 1997). Although fluid boiling was only recorded by fluid inclusions in the hydrothermal quartz, it likely also took place during uraninite precipitation at the site of mineralization. Fluid boiling has been proposed as a potential ore precipitation mechanism for uranium deposits, including vein-type uranium mineralization in the Beaverlodge area north of the Athabasca Basin (Liang et al. 2017) and the End uranium deposit associated with the Thelon Basin (Chi et al., 2017). The high fluid salinity recorded by the fluid inclusions suggests that uranium was dominantly transported as Cl complexes, as has been proposed for the unconformity-related uranium deposits in general (Komninou and Sverjensky, 1996; Richard et al., 2012). Assuming U was dissolved as Cl complexes in acidic brine (Richard et al., 2012) and knowing Cl is concentrated in the brine during boiling, U is likely partitioned into the liquid phase and depleted in the vapor phase. The preferential partitioning of non-aqueous volatiles into the vapor phase during boiling would decrease the pH of the ore-forming fluids (Drummond and Ohmoto, 1985), which could in turn dramatically decrease the solubility of uranium (Richard et al., 2012) while increasing the solubility of quartz (i.e., dissolution of quartz). Thus, the alternation between boiling and non-boiling in relation to fluid pressure fluctuation, as discussed above, may be related to the alternating uranium mineralization (and desilicification) and silicification inferred from the petrographic study.

Based on the above discussions about fluid temperature, pressure, boiling and ore precipitation, the mineralization and associated silicification and desilicification processes of the Phoenix uranium deposit may be envisaged as follows (Fig. 13). The burial depth at the time of mineralization is estimated to be around 2.5 km. Before the onset of the hydrothermal – mineralization event, the ambient temperature at the site of mineralization was about 110 °C and the fluid pressure was about

250 bar (hydrostatic) (t0 in Fig. 13A and B). As faulting along the WS fault took place, hydrothermal fluids were channeled along the fault zone, and the fluid temperature was higher than that of the background (t1 in Fig. 13A), whereas fluid pressure was instantly lowered to sub-hydrostatic values (t1 in Fig. 13B). The lowering of fluid pressure induced fluid boiling, which in turn caused an increase in pH value (t1b in Fig. 13C) relative to the incoming ore-forming fluid that is characterized by low pH (t1a in Fig. 13C). Reaction of the U-carrying fluid with reducing agents within the ore zone caused precipitation of uraninite (t1a in Fig. 13D), which is further augmented by pH increase due to fluid boiling (t1b in Fig. 13D). In the ore zone, the relatively high temperature, coupled with episodically increased pH values due to fluid boiling, resulted in significant desilicification and lack of quartz precipitation (Fig. 13E). In contrast, in the area outward from the ore zone, increased silica content carried over from the desilicification in the ore zone, combined with decreasing temperature, resulted in quartz precipitation (i.e., formation of hydrothermal quartz). Nevertheless, pH fluctuation in relation to fluid boiling resulted in alternating quartz precipitation and dissolution (t1 in Fig. 13E). However, little uraninite precipitation is associated with the desilicification events in this zone (Fig. 13D) despite the pH increase and temperature decrease, because uranium had been used up in the ore zone. In summary, the combined effect of T, P, boiling and pH change from the ore zone outward is such that there is net precipitation of uraninite and dissolution of quartz in the ore zone, and a net precipitation of quartz (despite episodic desilicification) and scarcity of uraninite precipitation in the silicification (hydrothermal quartz) zone.

7. Conclusions

Petrographic studies of the Phoenix uranium deposit indicate that the hydrothermal system associated with mineralization was characterized by alternating periods of “desilicification + clay (mainly tourmaline) alteration + uraninite precipitation” and silicification. Fluid inclusion studies of the hydrothermal quartz record development of H₂O-NaCl-CaCl₂ ± MgCl₂ fluids with a compositional continuum between NaCl-dominated and CaCl₂-dominated end members, which is common for unconformity-related uranium deposits, and is consistent with the “diagenetic-hydrothermal” model in which the mineralizing fluids were brines derived from the basin. However, the relatively low fluid inclusion homogenization temperatures (~90 to ~160 °C) documented in this study, together with regional stratigraphic data, suggest that the mineralization probably took place in a relatively shallow-burial (~2.5 km) rather than deep-burial (> 5 km) environment as invoked in the conventional model. Furthermore, coexistence of bi-phase aqueous fluid inclusions with various vapor percentages and monophasic vapor-only inclusions within individual fluid inclusion assemblages indicates fluid boiling, which is related to abrupt pressure drop due to fracturing. The formation of the Phoenix deposit may be related to episodic reactivation of the basement faults and associated fluid pressure fluctuation (hydrostatic to sub-hydrostatic), pH changes and fluid flow.

Acknowledgements

This research was financially supported by the TGI-4 (Targeted Geoscience Initiative Phase 4) uranium ore systems project from Natural Resources of Canada to Chi and Bethune and an NSERC-Discovery Grant to Chi. Denison Mines Corp. is thanked for accommodation and other logistical support during our fieldwork. Morteza Rabiei's assistance in sampling and part of the petrographic work is much appreciated. We are grateful for the detailed reviews by Kevin Ansdell and three other reviewers which greatly improved the quality of this paper.

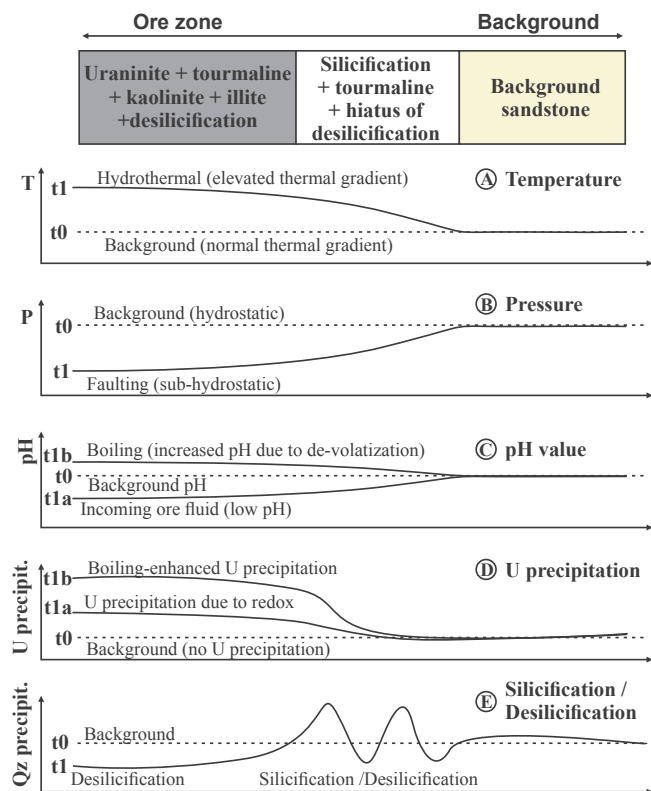


Fig. 13. A schematic model showing the spatial and temporal variation of fluid temperature (A), pressure (B), pH value (C), uraninite precipitation (D) and silicification/desilicification (E) in the hydrothermal system related to the Phoenix unconformity-related uranium deposit.

References

- Adlakha, E.E., Hattori, K., 2016. Paragenesis and composition of tourmaline types along the P2 fault and McArthur River uranium deposit, Athabasca Basin, Canada: *Can. Mineral* 54, 661–679.
- Alexandre, P., Kyser, K., Polito, P., Thomas, D., 2005. Alteration mineralogy and stable isotope geochemistry of Paleoproterozoic basement-hosted unconformity-type uranium deposits in the Athabasca Basin, Canada. *Econ. Geol.* 100, 1547–1563.
- Annesley, I.R., Madore, C., Portella, P., 2005. Geology and tectonotectonic evolution of the western margin of the Trans-Hudson Orogen: evidence from the eastern sub-Athabasca basement. *Saskatchewan. Can. J. Earth Sci.* 42, 573–597.
- Arseneau, G., Revering, C., 2010. Technical Report on the Phoenix Deposit (zones A & B)-Wheeler River project, Eastern Athabasca Basin, Northern Saskatchewan, Canada, NI 43-101 Report.
- Bakker, R.J., 2003. Package FLUIDS 1. Computer programs for analysis of fluid inclusion data and for modeling bulk fluid properties. *Chem. Geol.* 194, 3–23.
- Bakker, R.J., Baumgartner, M., 2012. Unexpected phase assemblages in inclusions with ternary H₂O-salt fluids at low temperatures. *Central Euro. J. Geosci.* 4, 225–237.
- Baumgartner, M., Bakker, R.J., 2009. CaCl₂-hydrate nucleation in synthetic fluid inclusions. *Chem. Geol.* 265, 335–344.
- Baumgartner, M., Bakker, R.J., 2010. Raman spectra of ice and salt hydrates in synthetic fluid inclusions. *Chem. Geol.* 275, 58–66.
- Blamey, N.J.F., 2012. Composition and evolution of crustal, geothermal and hydrothermal fluids interpreted using quantitative fluid inclusion gas analysis. *J. Geochem. Explor.* 116–117, 17–27.
- Blamey, N.J.F., Parnell, J., Longerich, H.P., 2012. Understanding detection limits in fluid inclusion analysis using an incremental crush fast scan method for planetary science. *LPSC #1038*.
- Blamey, N.J.F., Parnell, J., McMahon, S., Mark, D., Tomkinson, T., Lee, M., Shivak, J., Izawa, M.R.M., Banerjee, N.R., Flemming, R.L., 2015. Evidence for methane in martian meteorites. *Nat. Commun.* 6, 7399.
- Bodnar, R.J., 1993. Revised equation and table for determining the freezing point depression of H₂O-NaCl solutions. *Geochim. Cosmochim. Acta* 57, 683–684.
- Bosman, S.A., Korness, J., 2007. Building Athabasca Stratigraphy: Revising, Redefining, and Repositioning. Summary of Investigations 2007, Volume 2, Saskatchewan Geological Survey, Saskatchewan Ministry of Energy and Resources, Misc. Rep. 2007-4.2, CD-ROM, Paper A-8, 29.
- Buseck, P.R., Beyssac, O., 2014. From organic matter to graphite: graphitization. *Elements* 10, 421–426.
- Card, C.D., 2012. The origins of anomalously graphitic rocks and quartzite ridges in the basement to the southeastern Athabasca Basin, Summary of Investigations 2012, Volume 2, Saskatchewan Geological Survey, Sask. Ministry of the Economy, Misc. Rep. 2012-4.2, Paper A-6 p. 15.
- Card, C.D., Pana, D., Portella, P., Thomas, D.J., Annesley, I.R., 2007. Basement rocks to the Athabasca Basin, Saskatchewan and Alberta. In: Jefferson, C.W., Delaney, G. (Eds.), EXTECH IV: Geology and Uranium EXploration TECHnology of the Proterozoic Athabasca Basin, Saskatchewan and Alberta. *Geol. Surv. Can., Bull.*, pp. 69–87.
- Chi, G., Chu, H., 2016. Unconformity-related uranium mineralization in the Athabasca Basin, Canada: deep burial diagenetic-hydrothermal or epithermal? Goldschmidt 2016 Conference (Yokohama, Japan, June 26 – July 1, 2016), Abstract Volume, p. 475.
- Chi, G., Lu, H., 2008. Validation and representation of fluid inclusion microthermometric data using the fluid inclusion assemblage (FIA) concept. *Acta. Petrol. Sin.* 9, 1945–1953.
- Chi, G., Ni, P., 2007. Equations for calculation of NaCl/(NaCl + CaCl₂) ratios and salinities from hydrohalite-melting and ice-melting temperatures in the H₂O-NaCl-CaCl₂ system. *Acta Petrol. Sinica* 23, 33–37.
- Chi, G., Bosman, S., Card, C., 2013. Numerical modeling of fluid pressure regime in the Athabasca basin and implications for fluid flow models related to the unconformity-type uranium mineralization. *J. Geochem. Explor.* 125, 8–19.
- Chi, G., Liang, R., Ashton, K., Haid, T., Quirt, D., Fayek, M., 2014a. Evidence of fluid immiscibility from uranium deposits in northern Saskatchewan and Nunavut and potential relationship with uranium precipitation. *GAC-MAC Abstracts* 37, 57.
- Chi, G., Chu, H., Scott, R., Chou, I.-M., 2014b. A new method for determining fluid compositions in the H₂O-NaCl-CaCl₂ system with cryogenic Raman spectroscopy. *Acta Geol. Sinica* 88, 1169–1182.
- Chi, G., Chu, H., Scott, R., Li, Z., 2015. Basin-scale hydrodynamic and fluid P-T-X characterization of the Athabasca basin (Canada) and significance for unconformity-related U mineralization. Proceeding of the 13th Biennial SGA Meeting, 24–27 August 2015, Nancy, France, p. 1793–1796.
- Chi, G., Haid, T., Quirt, D., Fayek, M., Blamey, N., Chu, H., 2017. Petrography, fluid inclusion analysis, and geochronology of the End uranium deposit, Kiggavik, Nunavut. *Canada. Mineral. Deposita* 52, 211–232.
- Chi, G., Li, Z., Chu, H., Bethune, K.M., Quirt, D.H., Ledru, P., Normand, C., Card, C., Bosman, S., Davis, W.J., Potter, E.G., 2018. A shallow-burial mineralization model for the unconformity-related uranium deposits in the Athabasca Basin. *Econ. Geol.* in press.
- Chu, H., Chi, G., Chou, I.-M., 2016. Freezing and melting behaviors of H₂O-NaCl-CaCl₂ solutions in fused silica capillaries and glass-sandwiched films: implications for fluid inclusion studies. *Geofluids* 16, 518–532.
- Cloutier, J., Kyser, K., Olivo, G.R., Alexandre, P., 2010. Contrasting patterns of alteration at the Wheeler River area, Athabasca Basin, Saskatchewan, Canada: Insights into the apparently uranium-barren Zone K alteration system. *Econ. Geol.* 105, 303–324.
- Cuney, M., Brouand, M., Cathelineau, M., Derome, D., Freiberger, R., Hecht, L., Kister, P., Lobaev, V., Lorilleux, G., Peiffert, C., Bastoul, A.M., 2003. What parameters control the high grade-large tonnage of the Proterozoic unconformity related uranium deposit? In: Cuney, M. (Ed.), *Uranium Geochemistry. Proceedings, Nancy, France*, pp. 123–126.
- Derome, D., Cathelineau, M., Cuney, M., Fabre, C., Lhomme, T., Banks, D.A., 2005. Mixing of sodic and calcic brines and uranium deposition at McArthur River, Saskatchewan, Canada: A Raman and laser-induced breakdown spectroscopic study of fluid inclusions. *Econ. Geol.* 100, 1529–1545.
- Drummond, S.E., Ohmoto, H., 1985. Chemical evolution and mineral deposition in boiling hydrothermal systems. *Econ. Geol.* 80, 126–147.
- Duan, Z., Moller, N., Weare, J.H., 1992a. An equation of state for the CH₄-CO₂-H₂O system: I. pure systems from 0 to 1000°C and 0 to 8000 bar. *Geochim. Cosmochim. Acta* 56, 2605–2617.
- Duan, Z., Moller, N., Weare, J.H., 1992b. An equation of state for the CH₄-CO₂-H₂O system: II. mixtures from 50 to 1000°C and 0 to 1000 bar; *Geochim. Cosmochim. Acta* 56, 2619–2631.
- Duan, Z., Moller, N., Weare, J.H., 1996. Prediction of the solubility of H₂S in NaCl aqueous solutions: an equation of state approach. *Chem. Geol.* 130, 15–20.
- Dubessy, J., Pagel, M., Beny, J.-M., Christensen, H., Hickel, B., Kosztolanyi, C., Poty, B., 1988. Radiolysis evidenced by H₂-O₂ and H₂-bearing fluid inclusions in three uranium deposits. *Geochim. Cosmochim. Acta* 52, 1155–1167.
- Earle, S.A.M., Sopuck, V.J., 1989. Regional litho-geochemistry of the eastern part of the Athabasca Basin uranium province, Saskatchewan, Canada. *Uranium Resources and Geology of North America. Int. Atomic Energy Agency, Technical Document TECDOC-500* 263–296.
- Goldstein, R.H., Reynolds, T.J., 1994. Systematics of fluid inclusions in diagenetic minerals. *Soc. Sediment. Geology. Short Course* 31, 199p.
- Hoeve, J., Quirt, D., 1984. Mineralization and host rock alteration in relation to clay mineral diagenesis and evolution of the Middle-Proterozoic, Athabasca Basin, northern Saskatchewan, Canada. *Saskatchewan Res. Council, SRC Techn. Rep.* 187, 187.
- Hoeve, J., Sibbald, T., 1978. On the genesis of Rabbit Lake and other unconformity-type uranium deposits in northern Saskatchewan. *Canada. Econ. Geol.* 73, 1450–1473.
- Hoffman, P.E., 1988. United plates of America, the birth of a craton: early Proterozoic assembly and growth of Laurentia. *Ann. Rev. Earth Planet Sci.* 16, 543–603.
- Jefferson, C., Thomas, D., Gandhi, S., Ramaekers, P., Delaney, G., Brisbin, D., Cutts, C., Quirt, D., Portella, P., Olson, R., 2007. Unconformity-associated uranium deposits of the Athabasca Basin, Saskatchewan and Alberta, in: Jefferson, C.W., Delaney, G. (Eds.), EXTECH IV: Geology and Uranium EXploration TECHnology of the Proterozoic Athabasca Basin, Saskatchewan and Alberta: *Geol. Surv. Can., Bull.* 588, 23–67.
- Kerr, W.C., 2010. The discovery of the Phoenix Deposit: a new high-grade, Athabasca Basin unconformity-type uranium deposit, Saskatchewan, Canada. *Spec. Publ. Soc. Econ. Geol.* 15 (Vol. II), 703–728.
- Kominou, A., Sverjensky, D.A., 1996. Geochemical modeling of the formation of an unconformity-type uranium deposit. *Econ. Geol.* 91, 590–606.
- Kotzer, T.G., Kyser, T.K., 1995. Petrogenesis of the Proterozoic Athabasca Basin, northern Saskatchewan, Canada, and its relation to diagenesis, hydrothermal uranium mineralization and paleohydrogeology. *Chem. Geol.* 120, 45–89.
- Kyser, K., Cuney, M., 2015. Basins and uranium and deposits, in: Kyser, K., Cuney, M. (Eds.), *Geology and Geochemistry of Uranium and Thorium Deposits. Mineralogical Association of Canada, Short-Course Volume* 46, pp. 225–304.
- Li, Z., Bethune, K.M., Chi, G., Bosman, S.A., Card, C.D., 2015. Topographic features of the sub-Athabasca Group unconformity surface in the southeastern Athabasca Basin and their relationship to uranium ore deposits. *Can. J. Earth Sci.* 52, 903–920.
- Li, Z., Chi, G., Bethune, K.M., 2016. The effects of basement faults on fluid convection and implications for the formation of unconformity-related uranium deposits in the Athabasca Basin, Canada. *Geofluids* 16, 729–751.
- Li, Z., Chi, G., Bethune, K.M., Thomas, D., Zaluski, G., 2017. Structural controls on fluid flow during compressional reactivation of basement faults: insights from numerical modeling for the formation of unconformity-related uranium deposits in the Athabasca Basin, Canada. *Econ. Geol.* 112, 451–466.
- Li, Z., Chi, G., Bethune, K.M., Eldursi, E., Thomas, D., Quirt, D., Ledru, P., 2018. Synchronous egress and ingress fluid flow related to compressional reactivation of basement faults: the Phoenix and Gryphon uranium deposits, southeastern Athabasca Basin, Saskatchewan, Canada. *Mineral. Deposita* 53, 277–292.
- Liang, R., Chi, G., Ashton, K., Blamey, N., Fayek, M., 2017. Fluid compositions and P-T conditions of vein-type uranium mineralization in the Beaverlodge uranium district, northern Saskatchewan, Canada. *Ore Geol. Rev.* 80, 460–483.
- Macdonald, C., 1985. Mineralogy and geochemistry of the sub-Athabasca regolith near Wollaston Lake. In: Sibbald TII, Petruk W (ed) *Geology of Uranium Deposits. Proceedings of the CIM-SEG Uranium Symposium, September 1981: The Canadian Institute of Mining and Metallurgy, Special Volume* 32:155–158.
- Mercadier, J., Richard, A., Cathelineau, M., 2012. Boron- and magnesium-rich marine brines at the origin of giant unconformity-related uranium deposits: ⁸¹B evidence from Mg-tourmalines. *Geology* 40, 231–234.
- O'Connell, I., Hattori, K., Chen, S., Adlakha, E.E., and Sorba, C., 2015. Characterization of tourmaline from the Maw Zone, Gryphon Zone, and sandstones above the Phoenix uranium deposits, Athabasca Basin, Saskatchewan: Geological Survey of Canada, Scientific Presentation 37, 1 poster. doi:10.4095/296916.
- Pagel, M., 1975. Détermination des conditions physico-chimiques de la silicification diagenétique des grès Athabasca (Canada) au moyen des inclusions fluides. *Comptes Rendus Série D* 280, 2301–2304.
- Pagel, M., Poty, B., Sheppard, S.M.F., 1980. Contribution to some Saskatchewan uranium deposits mainly from fluid inclusion and isotopic data. In: Ferguson, S., Goleby, A. (Eds.), *Uranium in the Pine Creek Geosyncline. International Atomic Energy Agency (IAEA), Vienna*, pp. 639–654.

- Polito, P.A., Kyser, T.K., Thomas, D., Marlatt, J., Drever, G., 2005. Re-evaluation of the petrogenesis of the Proterozoic Jabiluka unconformity-related uranium deposit, Northern Territory, Australia. *Miner. Deposita* 40, 257–288.
- Rabiei, M., Chi, G., Normand, C., Davis, W.J., Fayek, M., Blamey, N., 2017. Hydrothermal REE (xenotime) mineralization at Maw Zone, Athabasca Basin, Canada, and its relationship with unconformity-related uranium deposits. *Econ. Geol.* 112, 1483–1507.
- Ramaekers, P., Jefferson, C.W., Yeo, G.M., Collier, B., Long, D.G.F., Drever, G., Mchardy, S., Jiricka, D., Cutts, C., Wheatley, K., Catuneanu, O., Bernier, S., 2007. Revised geological map and stratigraphy of the Athabasca Group, Saskatchewan and Alberta, in: Jefferson, C.W., Delaney, G. (Eds.), EXTECH IV: Geology and Uranium EXploration TECHNOlogy of the Proterozoic Athabasca Basin, Saskatchewan and Alberta: *Geol. Surv. Can., Bull.* 588, 155–192.
- Richard, A., Banks, D.A., Mercadier, J., Boiron, M.-C., Cuney, M., Cathelineau, M., 2011. An evaporated seawater origin for the ore-forming brines in unconformity-related uranium deposits (Athabasca Basin, Canada): Cl/Br and $\delta^{37}\text{Cl}$ analysis of fluid inclusions. *Geochim. Cosmochim. Acta* 75, 2792–2810.
- Richard, A., Rozsypal, C., Mercadier, J., Cuney, M., Boiron, M.-C., Cathelineau, M., Banks, D.A., 2012. Giant uranium deposits formed from exceptionally uranium-rich acidic brines. *Nature Geosci.* 5, 142–146.
- Richard, A., Boulvais, P., Mercadier, J., Boiron, M.-C., Cathelineau, M., Cuney, M., France-Lanord, C., 2013. From evaporated seawater to uranium-mineralizing brines: Isotopic and trace element study of quartz-dolomite veins in the Athabasca system. *Geochim. Cosmochim. Acta* 113, 38–59.
- Richard, A., Kendrick, M.A., Cathelineau, M., 2014. Noble gases (Ar, Kr, Xe) and halogens (Cl, Br, I) in fluid inclusions from the Athabasca Basin (Canada): Implications for unconformity-related U deposits. *Precamb. Res.* 247, 110–125.
- Richard, A., Cathelineau, M., Boiron, M.-C., Mercadier, J., Banks, D.A., Cuney, M., 2016. Metal-rich fluid inclusions provide new insights into unconformity-related U deposits (Athabasca Basin and Basement, Canada). *Mineral. Deposita* 51, 249–270.
- Richter, L., Diamond, L.W., Atanasova, P., Banks, D.A., Gutzmer, J., 2018. Hydrothermal formation of heavy rare earth element (HREE) – xenotime deposits at 1000°C in a sedimentary basin. *Geology* 2018 (in press).
- Roedder, E., 1984. Fluid inclusions. *Geol. Soc. Am. Bull.* 12, 644.
- Roedder, E., Bodnar, R.J., 1997. Fluid inclusion studies of hydrothermal deposits. In: Barnes, H.L. (Ed.), *Geochemistry of hydrothermal ore deposits*, 3rd edition. John Wiley & Sons, New York, pp. 657–698.
- Roscoe, W., 2014. Technical report on a mineral resource estimate update for the Phoenix uranium deposits; Wheeler River project, Eastern Athabasca Basin, Northern Saskatchewan, Canada. NI 43-101 technical report prepared for Denison Mines Corp., by Roscoe Postle Associates Inc., 134 p.
- Rosenberg, P.E., Foit, F.F., 2006. Magnesio-foitite from the uranium deposits of the Athabasca Basin, Saskatchewan, Canada. *Canadian Mineralogist* 44, 959–965.
- Sibson, R.H., 1987. Earthquake rupturing as a mineralizing agent in hydrothermal systems. *Geology* 15, 701–704.
- Sibson, R.H., 1987. Earthquake rupturing as a mineralizing agent in hydrothermal systems. *Geology* v. 15, 701–704.
- Sibson, R.H., Robert, F., Poulsen, K.H., 1988. High angle reverse faults, fluid pressure cycling, and mesothermal gold-quartz deposits. *Geology* 16, 551–555.
- Steele-MacInnis, M., Bodnar, R.J., Naden, J., 2011. Numerical model to determine the composition of $\text{H}_2\text{O-NaCl-CaCl}_2$ fluid inclusions based on microthermometric and microanalytical data. *Geochim. Cosmochim. Acta* 75, 21–40.
- Weatherley, D.K., Henley, R.W., 2013. Flash vaporization during earthquakes evidenced by gold deposits. *Nat. Geosci.* 6, 294–298.
- Wilde, A.R., Mernagh, T.P., Bloom, M.S., Hoffmann, C.F., 1989. Fluid inclusion evidence on the origin of some Australian unconformity-related uranium deposits. *Econ. Geol.* 84, 1627–1642.
- Yeo, G.M., Delaney, G., 2007. The Wollaston Supergroup, stratigraphy and metallogeny of a Paleoproterozoic Wilson cycle in the Trans-Hudson Orogen, Saskatchewan, in: Jefferson, C.W., Delaney, G. (Eds.), EXTECH IV: Geology and Uranium EXploration TECHNOlogy of the Proterozoic Athabasca Basin, Saskatchewan and Alberta: *Geol. Surv. Can., Bull.* 588, 89–117.